Wave, Tide and Topographical Controls on Headland Sand Bypassing

E. V. King[1, 2], D. C. Conley[1], G. Masselink[1], N. Leonardi[3], R. J. McCarroll[1], T. Scott[1], N. G. Valiente[4]

[1]Coastal Processes Research Group, School of Biological and Marine Sciences, Plymouth University, Plymouth, UK.

[2]Scottish Environment Protection Agency, Glasgow, UK.

[3]Department of Geography and Planning, School of Environmental Sciences, University of Liverpool, Liverpool, UK.

[4]Met Office, Fitzroy Road, Exeter, Devon, UK.

Corresponding author: Erin King (erin.king@plymouth.ac.uk)

Key Points:

1. Headland bypassing is potentially widespread on energetic embayed coasts.
2. Bypassing can be predicted for realistic morphology and sand coverage; key parameters are headland extent, surf zone width and toe depth.
3. Tides are a secondary control on bypassing rate under energetic waves. Wave-current interactions can dominate bypassing for median waves.

Key Words:

Headland bypassing, sediment transport, Delft3D, sediment budget, wave-current interactions, embayed beaches, wave-tide interactions, sediment availability.

Abstract

Embayed beaches separated by irregular rocky headlands represent 50% of global shorelines. Quantification of inputs and outflows via headland bypassing is necessary for evaluating long-term coastal change. Bypassing rates are predictable for idealised headland morphologies; however, it remains to test the predictability for realistic morphologies, and to quantify the influence of variable morphology, sediment availability, tides and waves-tide interactions. Here we show that headland bypassing rates can be predicted for wave-dominated conditions, and depend upon headland cross-shore length normalised by surf zone width, headland toe depth and spatial sediment coverage. Numerically modelled bypassing rates are quantified for 29 headlands under variable wave, tide and sediment conditions along 75km of macrotidal, embayed coast. Bypassing is predominantly wave-driven and nearly ubiquitous under energetic waves. Tidal elevations modulate bypassing rates, with greatest impact at lower wave energies. Tidal currents mainly influence bypassing through wave-current interactions, which can dominate bypassing in median wave conditions. Limited sand availability off the headland apex can reduce bypassing by an order of magnitude. Bypassing rates are minimal when cross-shore length > 5 surf zone widths. Headland toe depth is an important secondary control, moderating wave impacts off the headland apex. Parameterisations were tested against modelled bypassing rates, and new terms are proposed to include headland toe depth and sand coverage. Wave-forced bypassing rates are predicted with mean absolute error of a factor 4.4. This work demonstrates wave-dominated headland bypassing is amenable to parameterisation and highlights the extent to which headland bypassing occurs with implications for embayed coasts worldwide.

Plain Language Summary

It is important to understand the inputs and outputs of sand to beaches to effectively predict long term coastal change. This study focuses on the movement of sand between embayed beaches, around headlands, known as headland bypassing. We use a numerical model of a highly energetic 75km stretch of coast to predict how much sand moves around the headlands under different wave and tide conditions. We find that bypassing is mostly driven by energetic waves. Changes in water level with the tide has a secondary effect. Tidal currents interact with waves, and this interaction drives bypassing when waves are less energetic. The coverage of sand was also important, with more bypassing if sand is present off the headland toe. The depth of water off the headland apex is an important control on bypassing rate. We test how well a formula to calculate bypassing works, and propose new terms to improve it. This work indicates headland bypassing is potentially ubiquitous along exposed embayed coasts globally.

1. Introduction

Embayed beaches separated by irregular rocky headlands represent around 50% of the world's shoreline and are important zones ecologically and commercially (Short & Masselink, 1999). Accurate determination of sediment budgets is necessary for prediction of coastal change over long timescales in these zones. It has been recognised that the traditional view of embayed beaches as closed littoral cells is not accurate for many embayments, where sediment can enter and exit the system via headland bypassing (Goodwin et al., 2013; Ribiero et al., 2017; Duarte et al., 2014; Valiente et al., 2019a, b; Vieira da Silva et al., 2016, 2018).

Headland bypassing is defined as the process of sand transport around headlands, which act as obstructions to longshore sediment transport, forced by wave, tide and wind action (Evans, 1943; Valiente et al., 2019; Vieira da Silva et al., 2016, 2018). Headland bypassing can be an important contribution to longshore sediment transport and hence influence coastal sediment budgets and management plans (Thom et al., 2018). Investigations of circulation and bypassing around engineering structures and inlets have been conducted (FitzGerald et al., 2000; Acworth & Lawson, 2012; Ab Razak et al., 2013; Scott et al., 2016a) whilst more recently studies have focussed on sand bypassing natural headlands (Goodwin et al., 2013; Ribiero et al., 2017; Duarte et al., 2014; George et al., 2015; Vieira da Silva et al., 2016, 2018; McCarroll et al., 2018; Valiente et al., 2020). Recent modelling works demonstrate bypassing rates are predictable for individual headlands (McCarroll et al., 2018; Valiente et al., 2020) and idealised headland morphologies (George et al., 2019; McCarroll et al., In Review), however it remains to test this predictability using a range of real headland morphologies, and to examine the influence of embayment morphology, sediment availability and tidal effects on sand bypassing rates.

Embayment morphology is an important control on embayment circulation. Circulation is influenced by embayment length, cross-shore headland extent and surf zone width, incident wave height, incident wave angle, tide state and local bathymetry (e.g. Castelle et al., 2016; McCarroll et al., 2016, 2018; Mouragues et al., 2020; Scott et al., 2016a). Embayment cellular circulation can involve one or two headland attached cellular rip currents, or a single cellular rip current at the centre of the embayment (Castelle et al., 2016). These rips are often referred to as 'mega-rips' (Akan et al., 2020; McCarroll et al., 2016, 2018; Short, 1985), and are associated with high-energy conditions with major storm events thought to be an important driving force of headland-attached rip bypassing (Short & Masselink, 1999). Embayment length is important in determining the flushing of the surf zone via headland rips with wider embayments allowing greater development of longshore drift in oblique wave conditions, resulting in stronger flushing at the downwave headland (Castelle & Coco, 2013). Goodwin et al. (2013) observed sensitivity of the cross-embayment sand transport pathway downdrift

of a headland to the dominant wave direction, and switching between cross-embayment and nearshore transport modes dependent upon incident wave modality and directional power.

Headland morphology is an important control on headland bypassing (McCarroll et al., 2020; McCarroll et al., In Review; Wiggins et al., 2019). It is key to quantify headland and embayment morphometric parameters in order to examine their influence on headland bypassing. Such measurements are non-trivial due to the fractal nature of rocky coastlines (Burrough, 1981). Embayment morphometric parameters have been quantified in studies of embayment circulation and rip channel morphology (Short & Masselink, 1999; Castelle & Coco, 2012), whilst Fellowes et al. (2019) quantify a range of embayment morphometric parameters and use these to produce a morphometric classification. Recommendations are made in McCarroll et al. (In Review) for a method to calculate headland morphometric parameters for use in headland bypassing predictions. George et al. (2015) classify headlands into eight classes based on geomorphic and bathymetric parameters, finding headland perimeter, apex sharpness and bathymetric expression to be most important for controlling headland bypassing under wave forcing. Of these headland classes, it was suggested only one acts as a barrier to sand transport under all conditions, indicating the potential ubiquity of headland sand bypassing. These efforts give a basis from which to derive headland and embayment morphometric parameters for the purposes of this study.

The classification and method presented by George et al. (2015) can be used to indicate likelihood of headland bypassing and bypassing direction under wave forcing, but does not give an indication of bypassing magnitude. Predictions of bypassing magnitude were initially proposed by McCarroll et al. (2018), where a headland-specific parameter was conceived based upon modelled daily sand bypassing of a macrotidal headland. George et al. (2019) found that bypassing is controlled by wave angle, headland size and grain size. Valiente et al. (2020) show that headland bypassing of multiple headlands is predictable as a function of offshore wave power, although this requires a computationally expensive numerical model to first calibrate a polynomial to each headland. By modelling headland bypassing of a large number of synthetic headlands, McCarroll et al. (In Review) demonstrated that headland bypassing Q_b can be parameterised as an initial approximation as a function of headland cross-shore extent X_{head} and surf zone width X_{surf}:

$$Q_{b\_Orig} = Q_0 \cdot e^{-\left(\frac{X_{head}}{X_{surf}}\right)^2}, \quad (1)$$

Where the unconstrained open coast longshore sediment flux Q_0 is estimated using van Rijn (2014):

$$Q_0 = 0.00018 \cdot K \cdot g^{0.5} \cdot \tan(\beta)^{0.4} \cdot D_{50}^{-0.6} \cdot H_{s,b}^{3.1} \cdot \sin(2\alpha_b), \quad (2)$$

In which K is a proxy for wave period where K is 1.5 for swell waves and 1 for wind waves, g is gravitational acceleration, tan(β) is beach slope, D_{50} is median grain size, $H_{s,b}$ is breaking wave height and α_b is breaking wave angle relative to shore-normal. This quantity has the benefit of being calculable without use of computationally expensive numerical techniques.

It remains to test the current headland bypassing parameterisation of McCarroll et al. (In Review) on a range of realistic headland morphologies. Additionally, circulation and bypassing can be influenced by embayment morphology and nearby headlands (Scott et al., 2016a; McCarroll, et al., 2018, In Review), sediment availability off the headland toe (George et al., 2019) and headland underwater bathymetric expression (George et al., 2015; McCarroll et al., In Review). The influences of bathymetric expression and sediment spatial variability in sand bypassing rates are yet to be quantified. Waves are the primary driver of headland sand bypassing based on observation and modelling studies (Goodwin et al., 2013; Vieira da Silva et al., 2018; McCarroll et al., 2018; George et al., 2019); however, tidal elevations and tidal currents play a secondary role (McCarroll et al., 2018, In Review). Uncertainty remains as to the influence of these variables and how they relate to headland bypassing in a manner which could be included in bypassing parameterisations.

This paper aims to test the applicability of existing headland bypassing parameterisations against realistic headland morphologies, and to expand the parameterisations to include the influence of headland underwater expression, sediment availability and embayment morphology. We also aim to quantify the impact of tides and non-linear wave-tide interactions on headland bypassing rates. The North Coast of Cornwall presents ideal conditions for this investigation, with a wide variety of embayed beaches separated by irregular and varied rocky headlands, energetic waves, spatially variable sand coverage and macrotidal regime (King et al., 2019a).

The following objectives will be addressed: (i) quantifying headland and embayment morphologies and sediment spatial variability across this region; (ii) determining sand bypassing rates for headlands along this coastline under various physical forcing conditions using a validated coupled hydrodynamic, wave and sediment transport model; (iii) testing the performance of the parameterisation as presented in McCarroll et al. (In Review) against realistic headland morphologies, and suggesting improvements; and (iv) examining the impact of tidal currents and wave-current interactions on headland bypassing relative to wave-only forcing.

2. Study Area

The North Coast of Cornwall is situated in the South West United Kingdom, on the Northwest European Continental Shelf (Figure 1). Resonant effects contribute to large tidal amplitudes over the whole Celtic shelf, with a mean spring tide range (MSTR) in the study area of ca. 5m in the Southwest and increasing to >7m at Hartland Point (Uncles, 2010). Modelled regional scale bed shear stresses, tidal residual currents and sand transport pathways indicate residual sand transport towards the northeast along this coastline, progressively weakening as it moves up coast (Pingree & Griffiths, 1979; Holt et al., 2001; Uncles, 2010; King et al., 2019a). Strong tidal currents (around 1.5 ms^{-1} at springs) drive a net residual current of up to 15 cms^{-1} towards the northeast immediately adjacent to large coastal promontories. This residual is broken up by multiple headland-bound embayments, resulting in areas of low residual tidal transport close to shore. In combined wave and tide conditions, sand transport is wave dominated for median waves in these areas where tidal forcing is weakest and is wave dominated across the whole North Coast under extreme waves (King et al., 2019a).

A 75-km stretch of this coast was selected for this study (Figure 1). This section of coastline is comprised of embayed beaches separated by irregular rocky headlands (29 embayments were selected for this study). Beaches in the study area are comprised of medium quartz sand (Prodger et al., 2016). These embayments comprise a wide range of wave exposures, embayment lengths, degrees of embaymentisation and headland morphologies. This coast is directly exposed to the Atlantic, bringing waves with potential fetch lengths of 6000km (Collins, 1987). Winter storm H_s at nearshore wave buoys along the North Coast can exceed 6m (Scott et al., 2016b). Average H_s based on a 10-year hindcast of WAM is ~1.5m along this section of coast, with H_s of ~2m further offshore (Bricheno et al., 2015; King et al., 2019a). The wave climate in the region has experienced an increase in extreme (99th percentile) H_s of up to 1% per annum between 1985 and 2008, and has also experienced an increase in winter wave height and interannual variability (Young et al., 2011; Castelle et al., 2018).

The large tidal range, high degree of wave exposure and diversity of headland and embayment morphologies make this a suitable site for an investigation into the impacts of different environmental and morphological forcing conditions on potential headland bypassing.

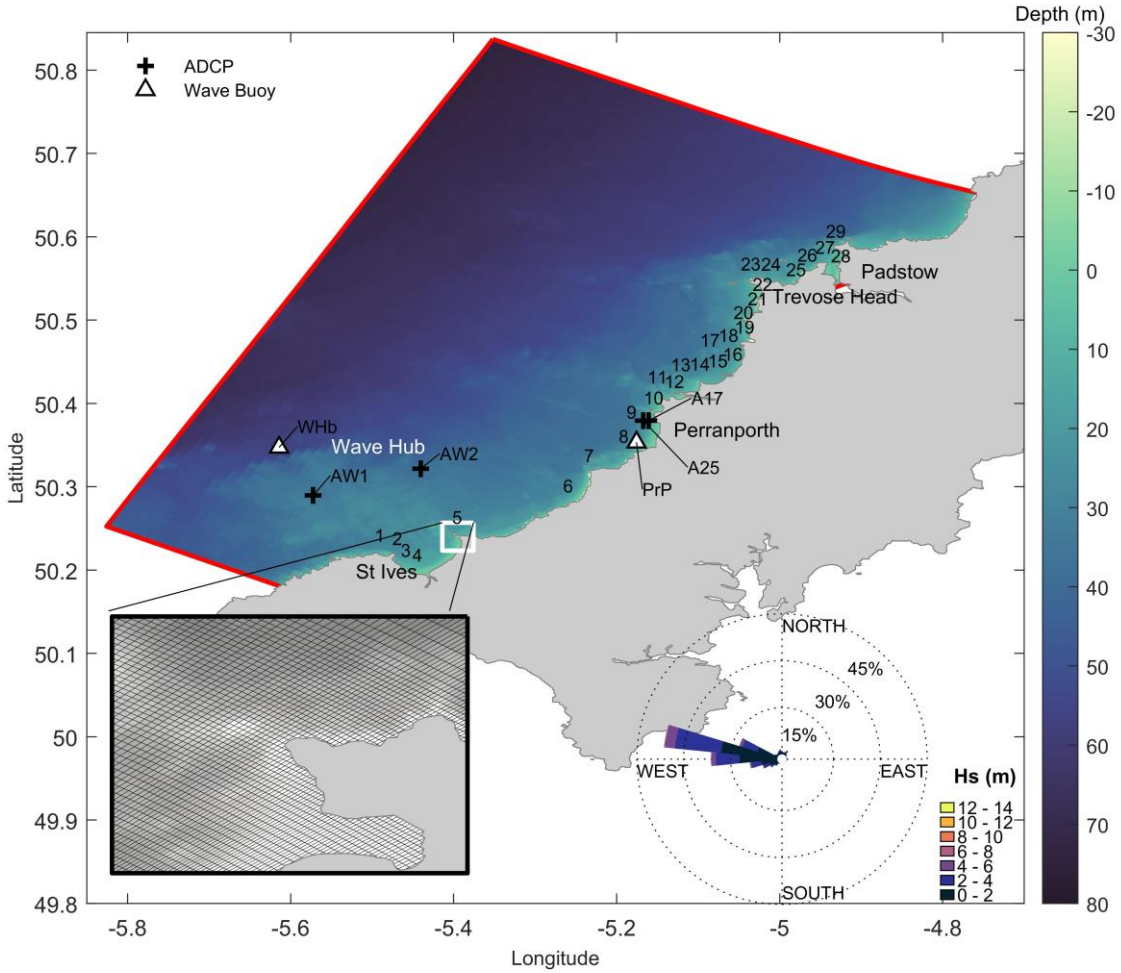

1. Clodgy Point
2. St Ives Head
3. Porthminster Point
4. Carrack Gladden
5. Godrevy Point
6. Porthtowan South
7. St Agnes Head
8. Cligga Head
9. Ligger Point
10. Penhale Point
11. Kelsey Head
12. Pentire Point West
13. Pentire Point East
14. Towan Head
15. Porth South
16. Trevelgue Head
17. Griffin's Point
18. Berryl's Point
19. Trenance Point
20. Park Head
21. Trethias
22. Treyarnon Point
23. Trevose Head
24. Cataclews Point
25. St Cadoc's Point
26. Gunver Head
27. Stepper Point
28. Trebetherick Point
29. Pentire Point

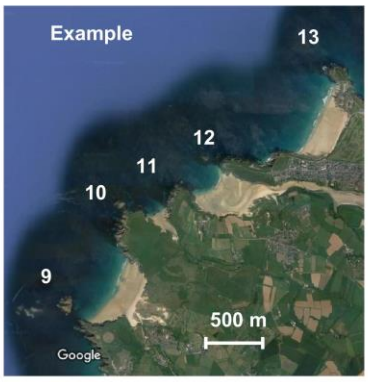

Figure 1: Map of the North Coast of Cornwall as represented within the model domain, showing the wave computational grid and bathymetry. The inset around Godrevy Point shows the computational grid as an example of the localised grid refinement around headlands. Headlands are numbered from southwest to northeast as indicated, and their names are included below the map. Other locations of reference are annotated. ADCP deployments (+) and wave buoy locations (Δ) are marked, alongside their name as referred to in the text. Open model boundaries are marked with a solid red line. A wave rose of the wave climate at the Wave Hub between 01-June-2015 and 31-May-2018 is inset bottom-right, showing principle wave directions. An example aerial image of headlands 9-13 is included for reference (bottom right). For the purpose of this study, upcoast is defined as towards the northeast (increasing headland number).

3. Methods

3.1. Numerical model

The process-based numerical model Delft 3D was used to model the North Coast (Figure 1). The FLOW hydrodynamic module was 2-way coupled to a SWAN third-generation spectral wave model packaged as Delft3D WAVE with an identical grid. Three-dimensional hydrodynamics are calculated using the unsteady shallow-water equations, following the Boussinesq approximation with the vertical momentum equation reduced to the hydrostatic pressure relation, assuming that vertical accelerations are small relative to gravitational acceleration (Lesser et al., 2004). The contribution of 3D turbulent eddies is modelled using a k-ε turbulence model. SWAN, packaged as Delft3D-WAVE, is a third-generation phase-averaged wave model based on fully spectral representation of the action balance equation, accounting for wave-current interaction through radiation stress, refraction, wind generation, whitecapping, nonlinear wave-wave interactions, bottom dissipation, and depth-induced breaking (Booij et al., 1999).

The North Coast model was one-way nested within a regional fully coupled hydrodynamic, wave and sand transport model validated and presented in King et al. (2019a). Grid resolution of the North Coast model was ca. 50m in the vicinity of headlands, and the model was run in 3D hydrodynamic mode with 10 sigma-levels in the vertical. The WAVE grid was extended two grid cells out from the FLOW grid. Bathymetry was derived from merged high-resolution multibeam data from the UK Hydrographic Office and lidar data Plymouth Coastal Observatory, corrected to Mean Sea Level 2000 datum using the Vertical Offshore Reference Frame (Turner et al., 2010) and merged with coarser EMODnet bathymetry offshore (EMODnet Bathymetry Consortium, 2016; Figure 1). Bathymetry at the boundaries matched the bathymetry of the regional forcing model. High-resolution bathymetry was assigned to the grid using spatial averaging, while lower resolution EMODnet bathymetry was assigned to the grid using triangular interpolation. A uniform grain size of 330μm (Prodger et al., 2017) throughout the domain was used, allowing cross-comparison of different embayments.

The hydrodynamic model has two water level boundaries and one velocity boundary to the south-west. This combination of forcing types provided the best agreement with observations during calibration. Boundaries were situated far from the headlands of interest. Boundary conditions were linearly interpolated from the regional model, which was itself one-way nested within the Atlantic Margin Model (FOAM-AMM7; McConnell et al., 2017; O'Dea et al., 2012). The hydrodynamic time-step was 12 s. Wind fields were interpolated linearly from 0.25° resolution scatterometer blended 6-hourly mean wind fields retrieved from the Copernicus Marine Service (Bentamy & Fillon, 2012).

Atmospheric pressure was interpolated linearly to the model grid from the 0.5° resolution Climate Forecast System version 2 model (Saha et al., 2014).

The wave model was forced with parametric boundary conditions (H_s, T_p, direction, directional spreading) linearly interpolated from the regional model at 1km resolution at the open boundaries. For calibration and validation the regional model in turn forced by the UK Met Office Wave Watch III continental shelf model (King, 2019a; Saulter, 2017). The wave time-step was 10 minutes, with a coupling interval between WAVE and FLOW of 1 hour, where wave forces are passed based on energy dissipation rate radiation stresses, bed shear stresses, Stokes drift and bottom orbital velocity, and receiving water levels and velocities. The wave model had a directional resolution of 5° (72 bins over a full circle) and 24 frequency bins between 0.05 and 1 Hz.

3.2. Sediments

Simulations were conducted under two bed composition scenarios: (i) a spatially uniform sediment coverage, to enable comparison of bypassing rates between different headlands; and (ii) a realistic sediment spatial distribution to highlight the role of sediment spatial availability on bypassing.

Sand transport rates were calculated using the TRANSPOR2004 formulation of Van Rijn (2004; 2007a, b). A single grain size of 330μm was used to enable comparison of bypassing rates between different headlands. The TRANSPOR2004 sediment transport formulation computes sediment transport contributions of suspended and bed load transport for both currents and waves, including their interactions. Enhancement of bed shear stress under currents and waves is accounted for in Delft3D following the method of Soulsby et al. (1993).

3.2.1. Spatially variable sediment distributions

To model the influence of spatial variability in sand coverage it is necessary to determine what locations in the domain are covered with sand or are exposed rock or gravel. Maps of spatial sediment classes available in the region such as the British Geological Survey product DiGBS250K are coarse, and unsuitable for modelling at the resolution required by this study. Consequently, an alternative method to determine sediment spatial variability was required. High-resolution (2m) UKHO bathymetry was used for this purpose. These data cover all embayments in this study. The bathymetry was resampled to 10m resolution for reasons of computational efficiency (Figure 2a). A 100m median filter was applied to generate a smoothed surface. This surface was subtracted from the resampled bathymetry (Figure 2b). The standard deviation of this surface was calculated over the same 100m square window, and the maximum of this standard deviation was calculated over this window (Figure 2c). This highlighted regions of rock across the domain. Polygonal areas of sediment in each embayment were then selected by eye roughly following the 0.2m threshold (Figure 2d).

This method assumes areas of sediment are vertically smoother than rock over a 100m window. Some sediment features were highlighted as rock due to their large vertical expression (such as large sandwaves west of St Ives). These were identifiable due to their linear, repeating pattern, and included in the sediment polygons. Perranporth has a sand-gravel transition at ca. -26m ODN (Valiente et al., 2019a). This was identifiable in the data as a border with elevated maximum standard deviation and was used to define to offshore sand polygon boundary. Similar borders elsewhere were also used for this purpose. The purpose of this was not to determine the exact spatial extent of sediment across this region, as this would require a more detailed observational campaign to determine sediment physical characteristics and spatial extent. Rather, the method was used as a means of generating an approximate sediment distribution to test the effect of a realistic pattern of sediment spatial coverage on headland bypassing rates *versus* a uniform, homogeneous sand bed. As such, this method was considered sufficient for the purpose of this study.

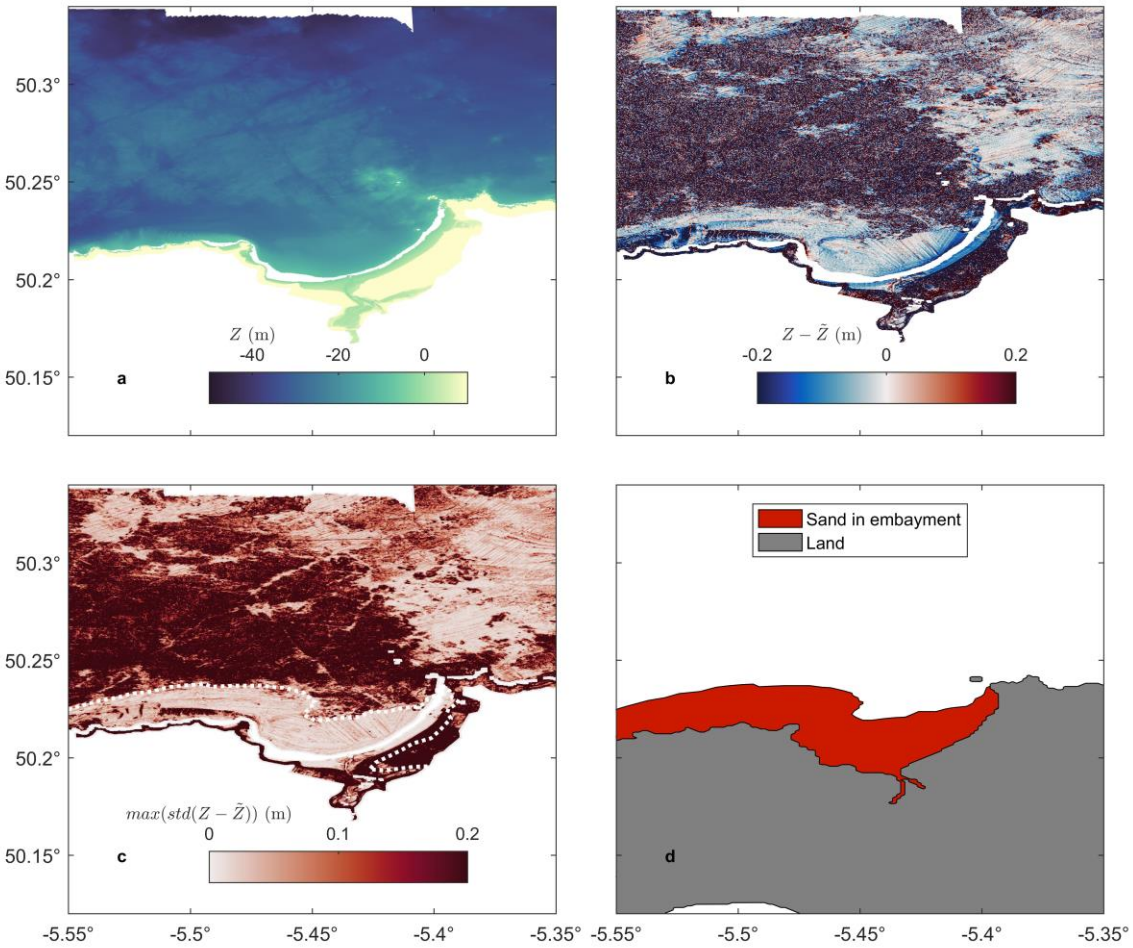

Figure 2: Sediment availability determination: example from St Ives Bay. (a) 10m resampled UKHO bathymetry. (b) The difference surface once a 100m window median filtered surface was subtracted from (a). (c) Maximum standard deviation of (b) over the same 100m window. Areas of high vertical variability are assumed to generally correspond to rock offshore. The selected sand-rock boundary is indicated with a white dashed line, corresponding to roughly the 0.2m contour offshore. (d)

Polygons of spatial sand extent in embayments of interest, determined by eye from (c), also indicating areas of land.

3.3. Calibration and validation

Numerical model calibration was performed using ADCP data at the Wave Hub, and wave buoy data at Perranporth (AW1/2 & PrP; Figure 1) over a 32-day window between 23/12/2013 and 24/01/2014, including three large storm events. Several boundary configurations were tested for the hydrodynamic model, and the best performing combination involved prescribing water levels at the offshore and northeast boundaries, and velocities at the southwest boundary. The Manning bottom friction formulation with a uniform roughness coefficient of 0.0275 performed best, as well as the Fredsøe (1984) bed shear stress formulation. Waves were calibrated for whitecapping formulations, bed friction formulations and bed friction coefficients. Calibration of these had a significant impact on wave model skill, with the default combination overestimating H_s at Perranporth. The best performing combination was the formulation of Komen et al. (1984) for whitecapping, Madsen et al. (1988) for bed friction, with a bed friction coefficient of 0.05. A full list of model formulations and parameters is included in Appendix A.

Validation of the model was performed for waves using wave buoys at Perranporth and Wave Hub, and for currents using ADCP derived currents offshore of the North headland of Perranporth (Figure 3; For locations, see Figure 1). Validation was performed over a 92-day period from 2016/06/01 to 2016/09/01 including an energetic event of 20th August. Time series in Figure 3 show a subset of the validation period for clarity. The tidal current axis is predominantly north-south oriented at the deployment sites, with very low east-west velocity components; therefore, only northward velocity components are shown in Figure 3. East-west components are validated and their skill metrics shown in Table 1.

Scatter plots in Figure 3 show all 2016 comparison data from which model skill was determined. Validation skill metrics are shown in Table 1. Skill was assessed using the following metrics: R^2, *BIAS*, mean absolute error *MAE*, Willmott Index of Agreement *WIA* and Brier Skill Score *BSS*. Equations for these metrics are included in Appendix B. Values of *BSS* ≥ 0.8 were considered excellent, ≥ 0.6 considered good, ≥ 0.3 considered reasonable, and < 0.3 considered poor.

In general, the model has good or excellent skill for both depth-integrated and near-bed instantaneous and residual (low-pass filtered) northward velocity components. The lowest performing residual northward velocity skill is the near-bed velocity at A17, which has “reasonable” skill. Eastward velocity components at both ADCP deployments were very small, which resulted in lower Brier Skill and R^2

metrics. A more informative metric at these sites is *WIA*: with -0.09 ≤ WIA ≤ 0.56 indicating the sum of the model error magnitudes is roughly equal to or less than the sum of the observed variability in the ADCP data, by half for a value of 0.5. The *MAE* for all velocity comparisons does not exceed 5 cms^{-1}.

The model has excellent skill for H_s and good skill for T_p. There is a slight northward bias in wave direction (~7° across all observations, increasing to ~14° at the Perranporth buoy). The *WIA* for wave direction indicates modelled errors are within the magnitude of observed variability about the mean direction (0.07 ≤ *WIA* ≤ 0.35).

Validation of sand transport rates is impossible due to a lack of observation data. McCarroll et al. (2018) applied sediment transport settings from the literature to model headland sand-bypassing at Perranporth (Figure 1). King et al. (2019a) used observed bedform asymmetry in high resolution bathymetric survey data and sand transport rates reported in the literature to validate their results, and found these settings performed adequately. The TRANSPOR2004 formulation (van Rijn 2007a, b) has been used successfully in other sand transport and headland bypassing studies (Grunnet et al., 2004; Luijendijk et al., 2017; McCarroll et al., 2018; Valiente et al., 2020). Accordingly, the settings included in Appendix A were used in this study.

Overall, good or excellent skill across most comparisons, and in particular, generally good or excellent skill predicting near-bed velocity components off the northern headland of Perranporth, indicates the suitability of this model to investigate sand transport at the coastal scale and headland bypassing.

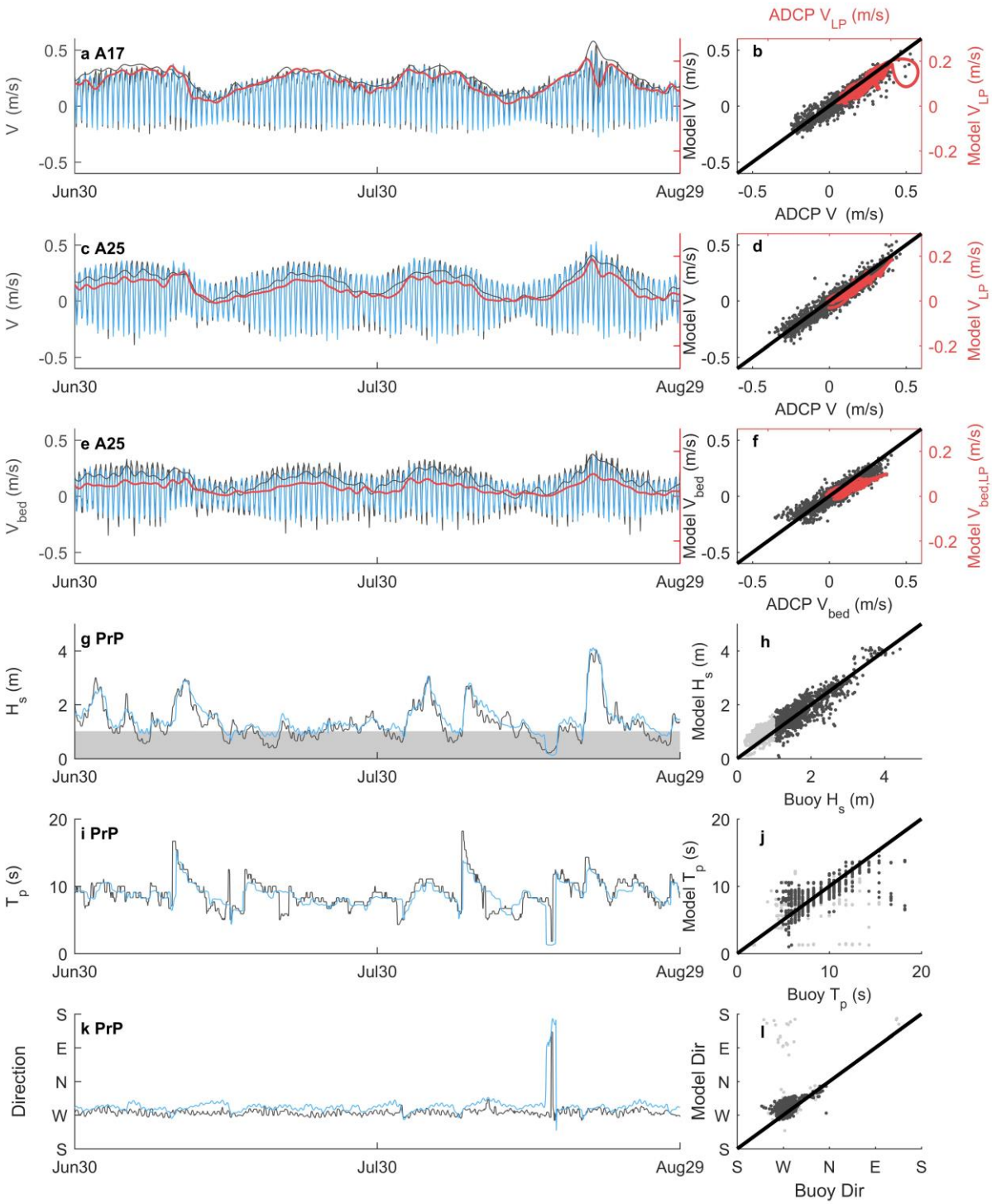

Figure 3: Validation time series and scatter plots. Observed time series are dark grey, modelled time series are blue. Where residual (low-pass) time series are shown, observations are dark grey and model data are red. Dark grey points in the scatter plots are hourly unfiltered data of model vs observation, red data are low-pass filtered data. **(a-d)** Depth-averaged northward velocity components from the Perranporth ADCP deployments A17 and A25. **(e, f)** Near bed northward velocity components at ADCP deployment A25. **(g, h)** Significant wave height at the Perranporth wave buoy. Data for H_s < 1m are highlighted in light grey here and in subsequent scatter plots. **(I, j)** Spectral peak wave period at the Perranporth wave buoy. **(k, l)** Mean wave direction at the Perranporth wave buoy. Wave buoy data are median filtered for clarity.

310

Table 1

Model Validation Statistics for Currents and Waves, including Residuals from Low-Pass Filtering.

Currents (ms^{-1})												
	Unfiltered Signal						Low-Pass Residual					
Location	N	R^2	BIAS	MAE	WIA	BSS	N	R^2	BIAS	MAE	WIA	BSS
A17-E	2208	0.04	3e-3	0.02	0.30	0.08	2208	0.02	2e-3	0.01	0.29	0.22
A17-N	2208	0.88	-0.01	0.03	0.83	**0.92**	2208	0.71	-0.01	0.02	0.69	**0.75**
A17-E (bed)	2208	0.01	-2e-3	0.02	0.31	0.09	2208	3e-3	-3e-3	0.01	0.14	-0.02
A17-N (bed)	2208	0.82	-0.02	0.04	0.75	**0.84**	2208	0.60	-0.02	0.02	0.55	*0.53*
A25-E	1538	0.06	-0.02	0.04	0.47	0.09	1538	3e-4	-0.02	0.02	-5e-3	-0.66
A25-N	1538	0.93	-0.02	0.04	0.87	**0.96**	1538	0.90	-0.02	0.02	0.71	**0.91**
A25-E (bed)	1538	0.05	-0.02	0.04	0.46	0.06	1538	0.01	-0.02	0.02	-0.09	-0.99
A25-N (bed)	1538	0.88	-0.02	0.05	0.81	**0.91**	1538	0.82	-0.02	0.03	0.61	**0.83**
ALL-E	3746	0.04	-0.01	0.03	0.48	0.16	3746	0.21	-0.01	0.01	0.56	*0.33*
ALL-N	3746	0.92	-0.02	0.03	0.85	**0.94**	3746	0.84	-0.02	0.02	0.72	**0.84**
ALL-E (bed)	3746	0.03	-0.01	0.03	0.43	0.10	3746	0.08	-0.01	0.02	0.39	-0.08
ALL-N (bed)	3746	0.85	-0.02	0.04	0.78	**0.88**	3746	0.73	-0.02	0.02	0.60	**0.66**

Waves														
	H_s (m)					T_p (H_s > 1m) (s)					*Dir* (H_s > 1m) (°)			
Location	N	R^2	BIAS	WIA	BSS	N	R^2	BIAS	WIA	BSS	R^2	BIAS	WIA	MAE
WHb	2168	0.86	0.32	0.66	**0.78**	1634	0.51	-0.14	0.70	**0.71**	0.01*	2.12	0.35	13.81
PrP	2207	0.83	0.14	0.74	**0.88**	1372	0.49	-0.12	0.70	**0.72**	0.26*	13.84	0.10	15.06
ALL	4375	0.87	0.24	0.71	**0.84**	3008	0.58	-0.15	0.73	**0.76**	0.04*	7.34	0.07	13.50

Note. Brier skill scores are coded for excellent and good (bold), reasonable (italic) and poor (underlined) model skill. Eastward and Northward velocity components are denoted by "-E" and "-N" respectively. Near-bed currents are denoted by "(bed)". "ALL" indicates performance for combined data from A17 and A25.

* Circular correlation coefficient for directional data.

3.4. Simulated scenarios

The wave climate was characterised near the offshore boundary using wave buoy data from the Wave Hub (Figure 1) over three years from 01-June-2015 to 31-May-2018. A Gumbel copula was fitted to the data for H_s and T_p to describe the joint probability distribution with H_s and T_p represented by gamma and rician marginal distributions respectively, following the method described in Genest et al. (2007; Figure 4). Marginal distributions were selected based on optimal performance minimising the Akaike Information Criterion. Joint $H_s \cap T_p$ conditions were selected from this distribution for exceedance probabilities of .50, .05 and.0014, the latter representing 12-hour exceedance. These predicted exceedances are in agreement with values for the region presented in the literature (Bricheno et al., 2015; King et al., 2019a; Scott et al., 2016b). Three modal wave directions were selected (Figure 4). Peak orbital velocities in the region are induced by swell wave action (Draper, 1967) and, consequently, scenarios presented here beyond calibration and validation exclude wind forcing.

Wave-only, tide-only and coupled wave-tide scenarios were conducted. Wave-only scenarios were conducted for two water levels corresponding approximately to spring high water (SHW) and spring low water (SLW) to give maximum variability in tidal elevations tested. Tidal scenarios were conducted over a spring-neap cycle and times where water levels were at Spring High or Spring Low were extracted for analysis. Velocities at these times ranged from 0.02 – 1 ms^{-1}. All scenarios were simulated for a uniform homogeneous sand bed and for the spatially variable sand distribution demonstrated in Figure 2. This resulted in a total of 56 scenarios for analysis.

Sand transport components were rotated to their along-shore and cross-shore components along each apex transect (Figure5) and these components were integrated from the headland apex to the maximum depth of transport (DoT; Valiente et al., 2019a) as a measure of instantaneous headland bypassing rate Q_b (m^3s^{-1}). Headlands have both an up-coast and down-coast transect defined by the beach orientation adjacent to each side of the headland (see Section 3.5). Bypassing was defined as positive up-coast (generally towards the northeast). Where bypassing rates at the two transects were divergent, bypassing was set to zero. There were no cases of convergent transport in the modelled bypassing rates. Sand transport rates lower than the range of validation presented in van Rijn (2007b) were set to zero prior to integration (0.00016 m^3/m/tidal cycle).

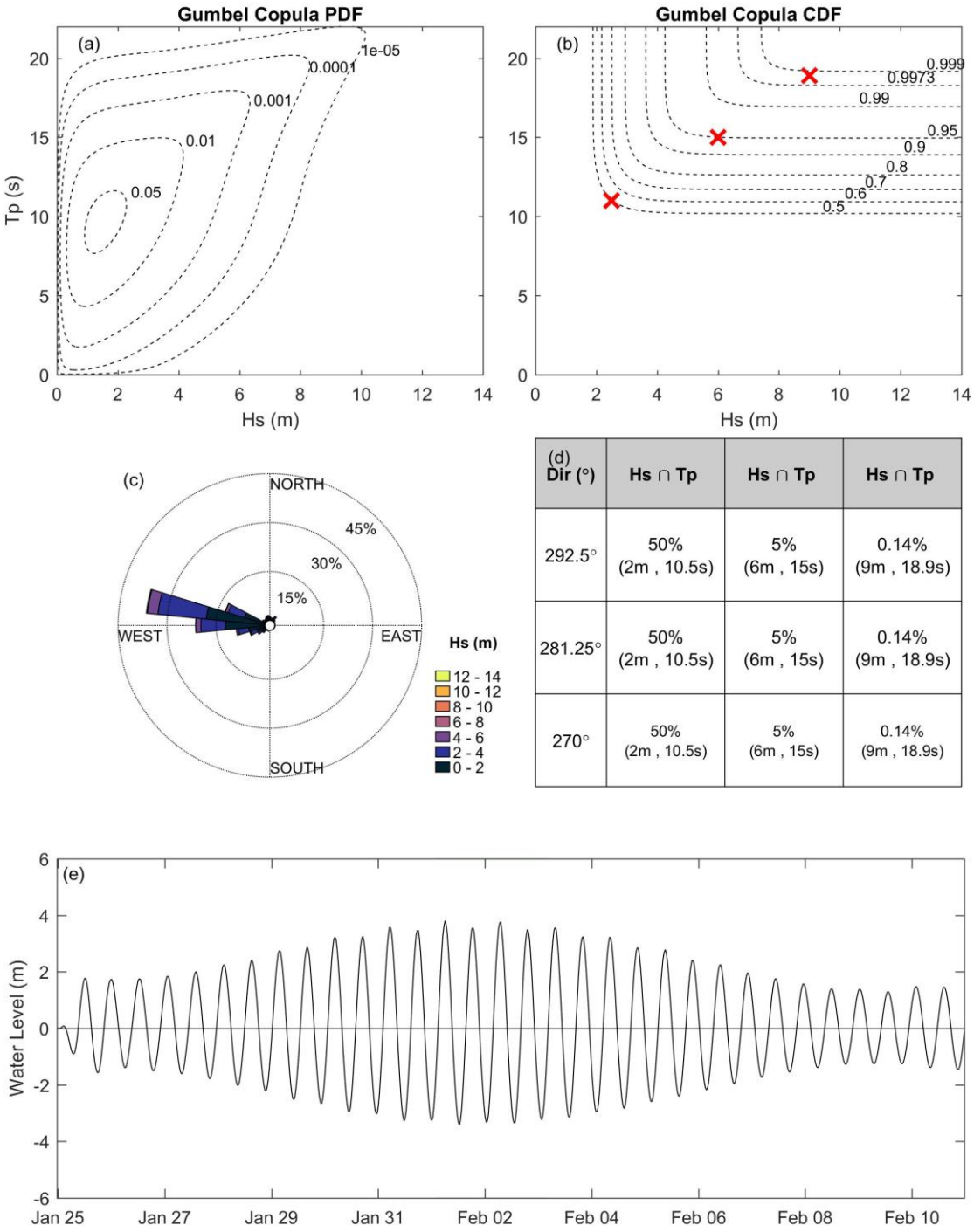

(d)

Dir (°)	Hs ∩ Tp	Hs ∩ Tp	Hs ∩ Tp
292.5°	50% (2m , 10.5s)	5% (6m , 15s)	0.14% (9m , 18.9s)
281.25°	50% (2m , 10.5s)	5% (6m , 15s)	0.14% (9m , 18.9s)
270°	50% (2m , 10.5s)	5% (6m , 15s)	0.14% (9m , 18.9s)

Figure 4: Wave climate characterisation used to select conditions for simulation. (a) Gumbel copula PDF representing the joint probability density of H_s and T_p. (b) Gumbel copula CDF representing the cumulative joint probability of H_s and T_p from which conditions were selected (red crosses). (c) Wave rose showing three modal wave directions from West to West-northwest. (d) Wave conditions selected for simulations. (e) Example tidal signal from Perranporth during the tide-only simulation. The first 7 days were used as model spin-up.

350

Wave-only scenarios were run for 72 hours, and sand transport was averaged over the final 24 hours. In tidal scenarios, times of spring high and low water were defined as when the median water level across each transect was > + 3m or < - 3m relative to mean sea level (MSL2000 datum) respectively. Tide range increases towards the northeast; therefore, the number of points satisfying this criteria increased moving up-coast. Bypassing rates were averaged over all times where the water level was within the SHW or SLW depth bin at each headland.

3.5. Quantifying morphometric and environmental parameters

Headland and embayment morphological parameters used are depicted in Figure 5. Headland morphology is measured in relation to the waterline around the headland for the water level under consideration, resulting in an apparent morphology that varies over a tidal cycle. Apparent cross-shore extent X_{head} is measured perpendicular to the orientation of the waterline on the up-wave beach adjacent to the headland, whilst longshore extent is measured parallel to the up-wave beach waterline (McCarroll et al., In Review). Thus, down-wave headland morphology is not considered.

Surf zone width is measured perpendicular to the beach waterline adjacent to the headland (Figure 5), from the beach waterline to the edge of the outer surf zone. For the purpose of this study, this was defined as the point at which the fraction of wave energy dissipation due to breaking reached 5%. This was derived from the model. Breaking wave height $H_{s,b}$ and direction at breaking α_b were then interpolated from the model at this point. Beach slope was also determined along this transect from the waterline to the DoT, taken from Valiente et al. (2019a).

Sediment coverage was considered between the headland adjacent transect and the headland apex transect. This adjacent transect was taken at 100m from the headland intersection with the beach, or at the midpoint of the beach if beach length L^b < 200m. Exploratory parameters included the cross-shore sediment extent X_{sed} and the area of sediment coverage adjacent to the headland A_{sed}. This was used to determine a ratio R_{sed} defined as:

$$R_{sed} = \frac{A_{sed}}{A_{DoT}}, \tag{3}$$

Where A_{DoT} is the total area between the adjacent and apex transects, bounded by the headland face and DoT. Depth off the headland toe Z_{toe} was determined 50m offshore of the headland apex along the apex transect. This was nondimensionalised across all headlands by dividing by 50m to give the slope of the headland toe m_t:

$$m_t = \frac{Z_{toe}}{50\ m}, \tag{4}$$

Embayment parameters were calculated in accordance with Fellowes et al. (2019) using the headland morphologies adjacent to the beach on either side of the bay to define the lateral boundaries of the embayment (Figure 5). Beach length L_b was calculated between the two headland faces using the point of intersection between the face and the beach, where the water level contour diverges from the beach line. For very small beach lengths where determination of the beach orientation at the resolution of the model was subject to greatest error, the orientation was determined from either the adjacent bay or the general orientation of that stretch of coastline.

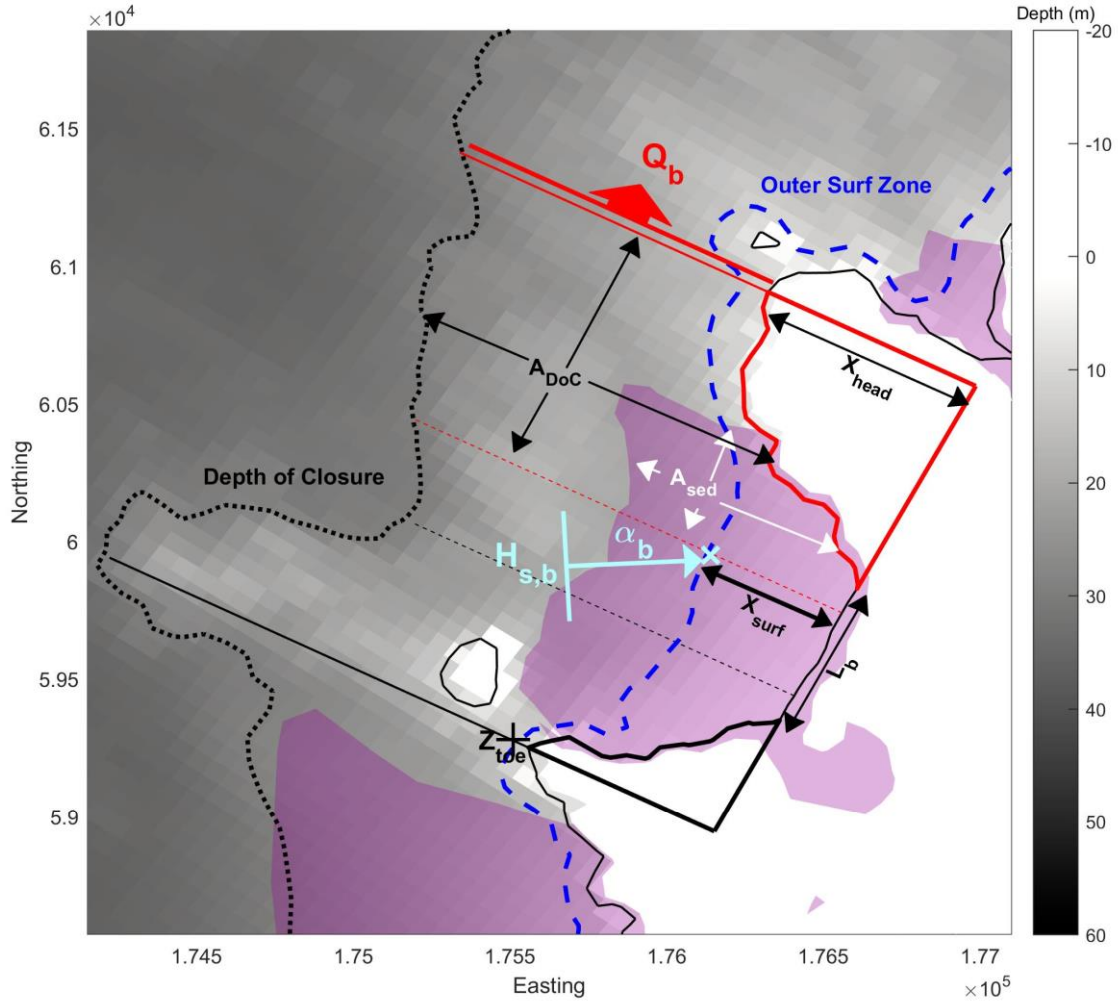

Figure 5: Example schematic of morphological and environmental parameters at Holywell Bay at spring high water. Apex transects (solid line) and adjacent beach transects (dashed line) are coloured by their respective headland. Parameters shown: Breaking wave angle α_b relative to shore normal, breaking wave height $H_{s,b}$, surf zone width X_{surf}, cross-shore headland length X_{head}, beach length L_b, headland toe depth Z_{toe}, sediment area adjacent to headland A_{sed}, total area between headland and maximum depth of transport A_{DoT}, and sand bypassing rate Q_b.

4. Results

4.1. Headland and embayment morphology

Selected quantified morphological parameters are displayed in Figure6 for each headland (a, c, e and g) with summary statistics shown using boxplots in (b, d, f and h). Parameters were quantified for upcoast and downcoast apparent morphologies for spring high and low water (SHW and SLW, respectively). For the purpose of this study, upcoast is defined as towards the northeast (increasing headland number). Headland morphology varies widely along this coast, and some headlands (4, 15, 16 & 22) cease to be apparent headlands at SLW, when the water line recedes beyond the headland apex. Headland cross-shore extent X_{head} (a, b) was seen to vary between ca. 40 m and 1800 m, and increase by around a factor 2 between SLW and SHW. X_{head}, defined relative to the waterline on the beach and at the headland apex (Figure 5), tended to be smaller upcoast than downcoast which may predispose this coastline towards upcoast bypassing. Toe depth Z_{toe} (c, d) varied between ca. 0.5 m and 17 m, and was fairly constant between up and downcoast morphologies, whilst increasing between SLW and SHW by ca. 3 – 4 m. Beach length L_b (e, f) varied between ca. 50 m to 7500 m, and decreased between SLW and SHW by around 1/3 on average. Sediment coverage R_{sed} (g, h) was distributed between full sediment coverage to the DoT and ca. 1 % coverage, and was similarly distributed between water levels and up and downcoast aspects. The wide range of morphologies represented here indicates the suitability of this region for testing the parameterisation of headland bypassing rates.

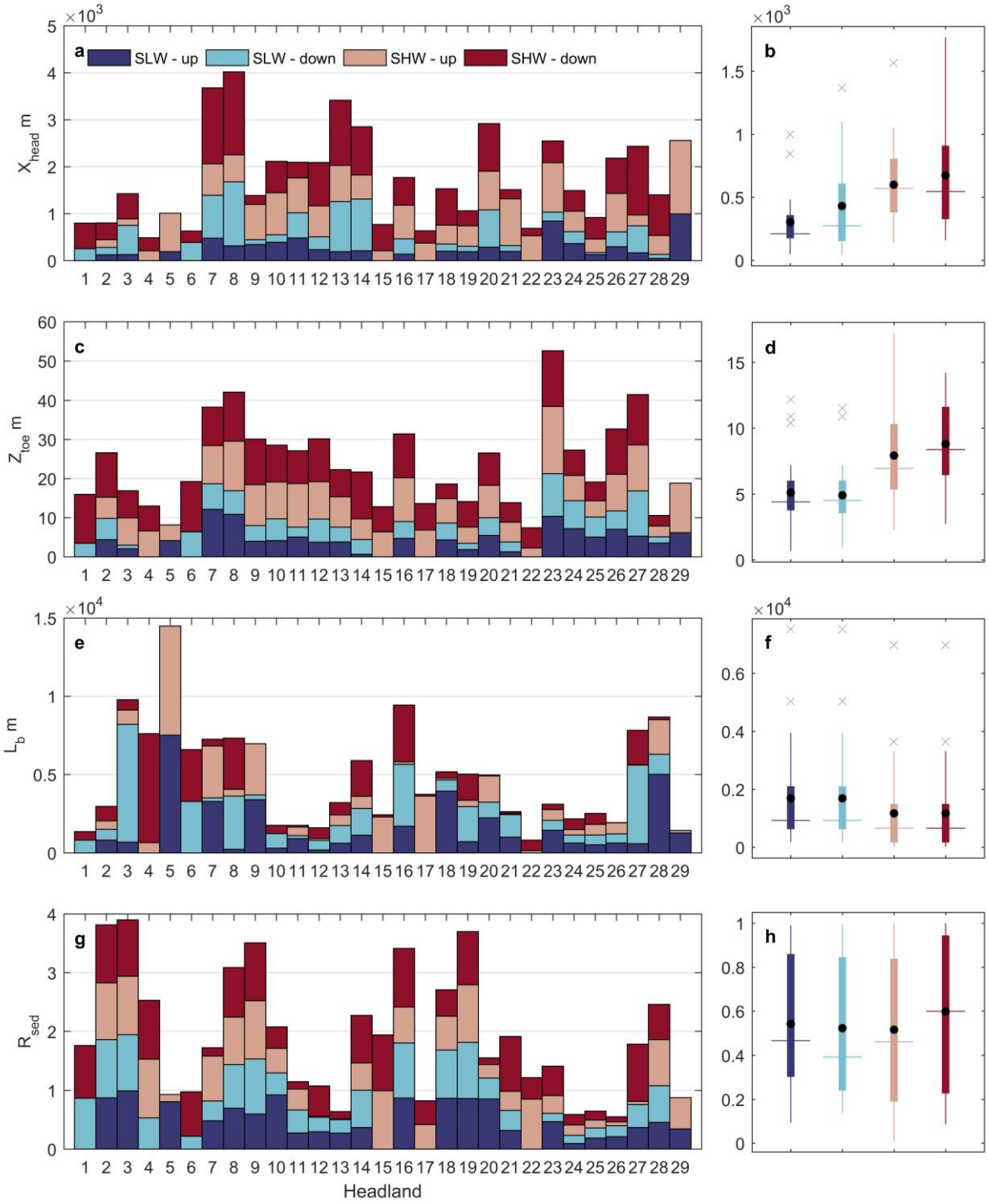

Figure 6: Summary figure of headland and bay morphological parameters including: headland cross-shore length X_{head}, headland toe depth Z_{toe}, beach length L_b and sediment ratio R_{sed}. Stacked bar graphs (a, c, e, g) show parameter values per headland for spring high water (SHW) and spring low water (SLW), and for the upcoast orientation (up) and downcoast orientation (down). Box plots (b, d, f, h) show summary statistics for each water level and headland orientation. The main body of the boxes span the 25th and 75th percentiles, the horizontal bar shows the median, the mean is shown (black dots), whiskers span up to 1.5 × inter quartile range, and outliers are shown (black crosses).

4.2. Headland bypassing

Headland bypassing was active across ~93% (27/29) of headlands for at least one wave condition under wave-only forcing. Only two headlands (5 – Godrevy Point & 23 – Trevose Head) were closed to wave-forced bypassing under all tested conditions. Headland bypassing was blocked for at least one incident wave direction for 41.4% (12/29) of headlands under median (50% exceedance) waves, for 27.6% (8/29) of headlands under large (5% exceedance) waves, and 24.1% (7/29) of headlands for extreme (12 hour exceedance) waves. More headlands exhibited upcoast bypassing than downcoast. In this section we quantify the influence of wave conditions, headland bathymetric expression, sediment spatial availability and tides. We test the performance of the parameterisation of McCarroll et al (In Review), and suggest improvements to account for bathymetric expression and non-uniform sediment coverage.

This section is subdivided into four parts: (1) starting with uniform sediment availability and wave-only forcing scenarios, we examine the influence of wave conditions and tidal elevations on bypassing rates; (2) we test the performance of the parameterisation of McCarroll et al. (In Review), and examine the effect of headland bathymetric expression; (3) we compare uniform and non-uniform sediment scenarios under wave-only forcing; and (4), we quantify the impact of tidal currents for uniform and non-uniform sediments, including wave-current interactions.

4.2.1. Effect of wave condition and tidal elevation

Bypassing rates for wave-only scenarios are shown in Figure 7a-c. For headlands 1 and 29 data were excluded if bypassing was into the region of interest from the model boundaries, as model resolution becomes poor beyond these headlands. Sequential headlands with positive bypassing rates indicate a potential wave-forced upcoast sand transport pathway, while sequential negative bypass rates indicate a potential downcoast transport pathway. Headlands with zero net bypassing (including cases with divergent transport) under all conditions (5, 23) are considered closed to wave-forced sand bypassing. Data for different tidal elevations are differentiated with solid and dashed lines for SHW and SLW respectively.

The impact of tidal elevation on headland bypassing rates was independent of wave direction (Figure 7a-c). The relative impact of tidal elevation changes was greatest during median wave conditions, where in some cases bypassing was activated only at SLW. In other cases, bypassing direction changed between SHW and SLW, mainly for median wave conditions. The impact of changing water levels decreases as wave height increases (Figure 7d). For median waves, bypassing at SLW has a median increase in magnitude of ca. 4 × relative to SHW, whereas this is reduced to ca. 2.5 × for large waves and ca. 1.5 × for extreme waves. The mean increase in bypassing at SLW is influenced by several large

441 outliers (beyond the axes scale) for median waves where bypassing increased from a very low level,
442 otherwise it is in close agreement with the median for large and extreme waves.

443 Bypassing rates were strongly dependent upon the cross-shore headland extent relative to surf zone
444 width (Figure7e), in agreement with prior literature on headlands and groynes (McCarroll et al., In
445 Review; Scott et al., 2016a). There was very little bypassing for $X_{head} > 5\ X_{surf}$ under all conditions, and
446 for $X_{head} > 3\ X_{surf}$ except where $\sin(2\alpha_b)$ was high indicating oblique wave angles conducive to strong
447 longshore transport. With a couple of exceptions, cases where bypassing was totally blocked fell
448 within the region of $X_{head} > 5\ X_{surf}$. Most data where bypassing was active in this region of $X_{head} > 5\ X_{surf}$
449 indicated very low bypassing rates of ca. 10^{-5} and 10^{-4} m^3s^{-1}, or approximately 1 – 10 m^3day^{-1}.

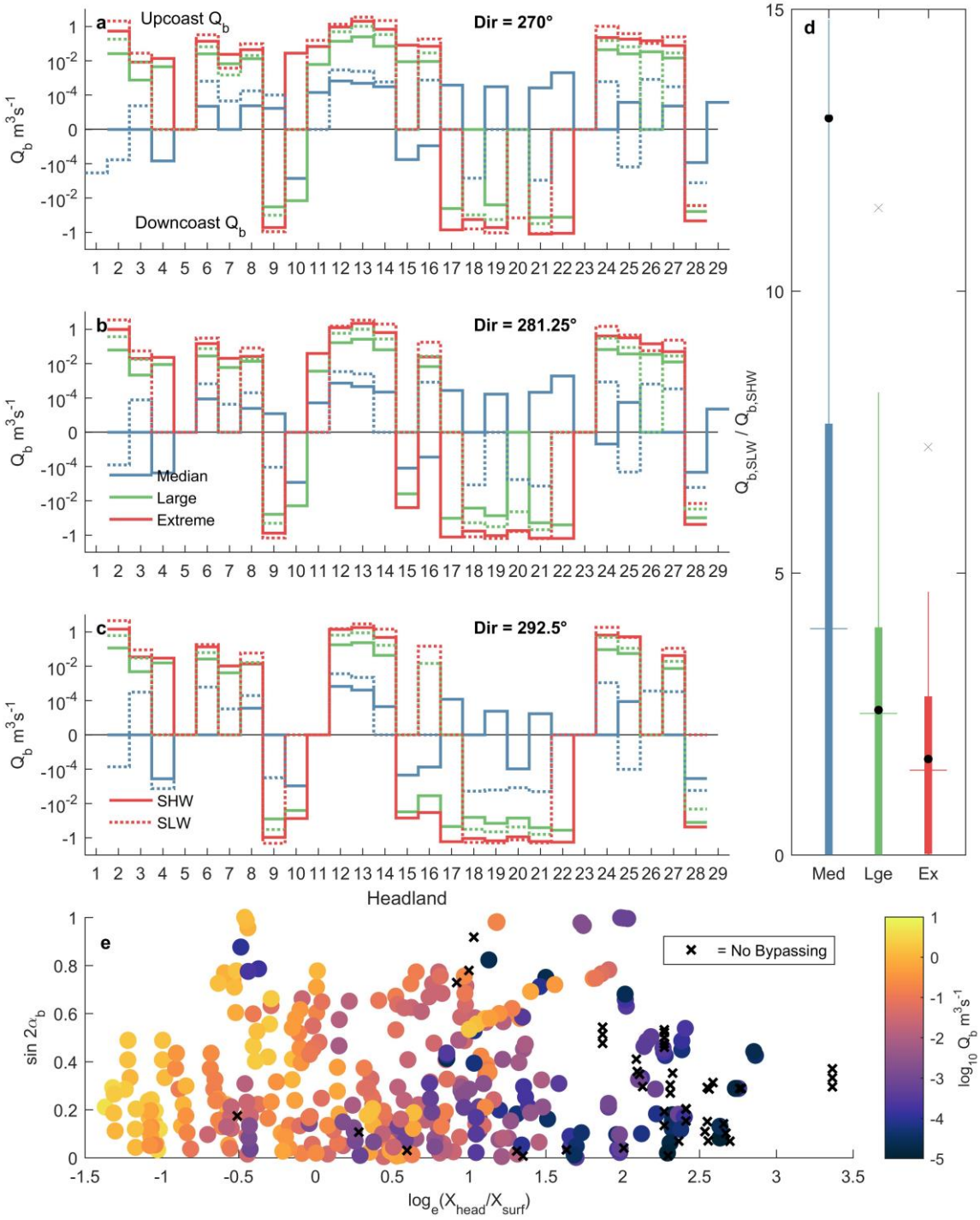

Figure 7: The influence of different wave conditions, wave direction and tidal elevation on headland bypassing rates for a uniform sand bed without tidal currents. (a-c) sand bypassing rates per each headland for median (blue), large (green) and extreme (red) wave conditions at spring high (solid) and low (dotted) water, and waves from (a) 270°, (b) 281.25° and (c) 292.5°. Y axes are a $\log_{10}$ scale. Positive (negative) values are indicative of upcoast (downcoast) bypassing. (d) Boxplots summarising the ratio of bypassing rates at spring low vs high water with median (horizontal line), mean (black dot) and whiskers indicating $1.5 \times IQR$. (e) Scatter diagram illustrating effect of wave breaking angle and surf zone width on bypassing rates using $\sin(2\alpha_b)$ and $\log_e(X_{head}/X_{surf})$. Colours show bypassing magnitude on a $\log_{10}$ scale. Crosses denote cases with no bypassing.

450

4.2.2. Parameterisation and the influence of bathymetry

The parameterisation of McCarroll et al., (In Review), based on idealised isolated headlands with uniform bathymetric expression and uniform sediment availability (Equations 1 & 2), was tested against the bypassing rates shown in Figure 7. These bypassing rates represent the most idealised conditions in this study, with uniform sediment availability and no tidal currents. Therefore, the primary differences in these data relative to the idealised conditions of McCarroll et al., (In Review) are the bathymetric expression of the headland below the water line and the proximity of adjacent headlands.

A comparison of the modelled headland bypassing rates versus the parameterisation in Equation 1 is shown in Figure 8a. This includes bypassing rates from all wave scenarios and water levels. Headland X_{head} was calculated separately for SHW and SLW, therefore this also represents the ability of the parameterisation to handle variability in tidal elevation. The original formulation greatly underestimates bypassing rates for the median wave conditions. A relatively minor alteration of the formulation of Equation 1 results in an improved fit to the bypassing rates predicted by the Delft3D model (Figure 8b), by changing the power in the exponent from 2 to 0.5 (Equation 5), effectively adjusting the slope of the exponential curve. This alteration mainly influences predictions in low-magnitude bypassing conditions where $X_{head} >> X_{surf}$, and its implications are discussed in Section 5. For $X_{head} < 0.5\ X_{surf}$ the parameterised bypassing rate was set to Q_0 (McCarroll et al., In Review).

$$Q_{b\_Adj} = Q_0 \cdot e^{-\left(\frac{X_{head}}{X_{surf}}\right)^{0.5}}, \quad (5)$$

There remains spread about the ideal fit 1:1 line with a MAE of a factor 4.3 and RMSE of a factor 6.5. This spread was hypothesised to be due to the influence of the variable bathymetric expression of the headlands and variable embayment morphology. A number of bathymetric and embayment morphological parameters were tested, including the bathymetric slope ratio of George et al. (2015), the beach length, headland separation, the degree of embaymentisation of Fellowes et al. (2019), headland longshore extent and headland toe depth in the form of m_t (Equation 4). Ultimately, the only parameter with a clear relationship to the deviation of the headland bypassing rates from the idealised solution was m_t (Figure 8c). An exponential term was fitted of the form:

$$Q_{b\_Toe} = Q_{b\_Adj} \cdot e^{a-\frac{1}{(m_t-b)^2}}, \quad (6)$$

Where a and b were calibration parameters. The best fit was found for a = 3.5 and b = 0.7, shown in Figure 8d. This improved the MAE of the parameter to a factor 3.5 and RMSE to a factor 5.2.

Bypassing directions were generally predicted correctly as a function of breaking wave direction relative to shore normal. The percentage of scenarios where bypassing was predicted correctly is shown in Figure 8e (grey bars) for each headland. Where there was no bypassing under any conditions, no bars are shown. Coloured bars with negative percentages indicate the percentage of scenarios where bypassing direction was wrongly predicted. The colours indicate the wave conditions where bypassing direction was predicted wrongly. For over half of headlands that had at least one bypassing direction wrongly predicted, the direction was wrong for median wave, low bypassing conditions or for only one or two scenarios. Six headlands had bypassing direction wrongly predicted for over 50% of cases. These are discussed in section 5.

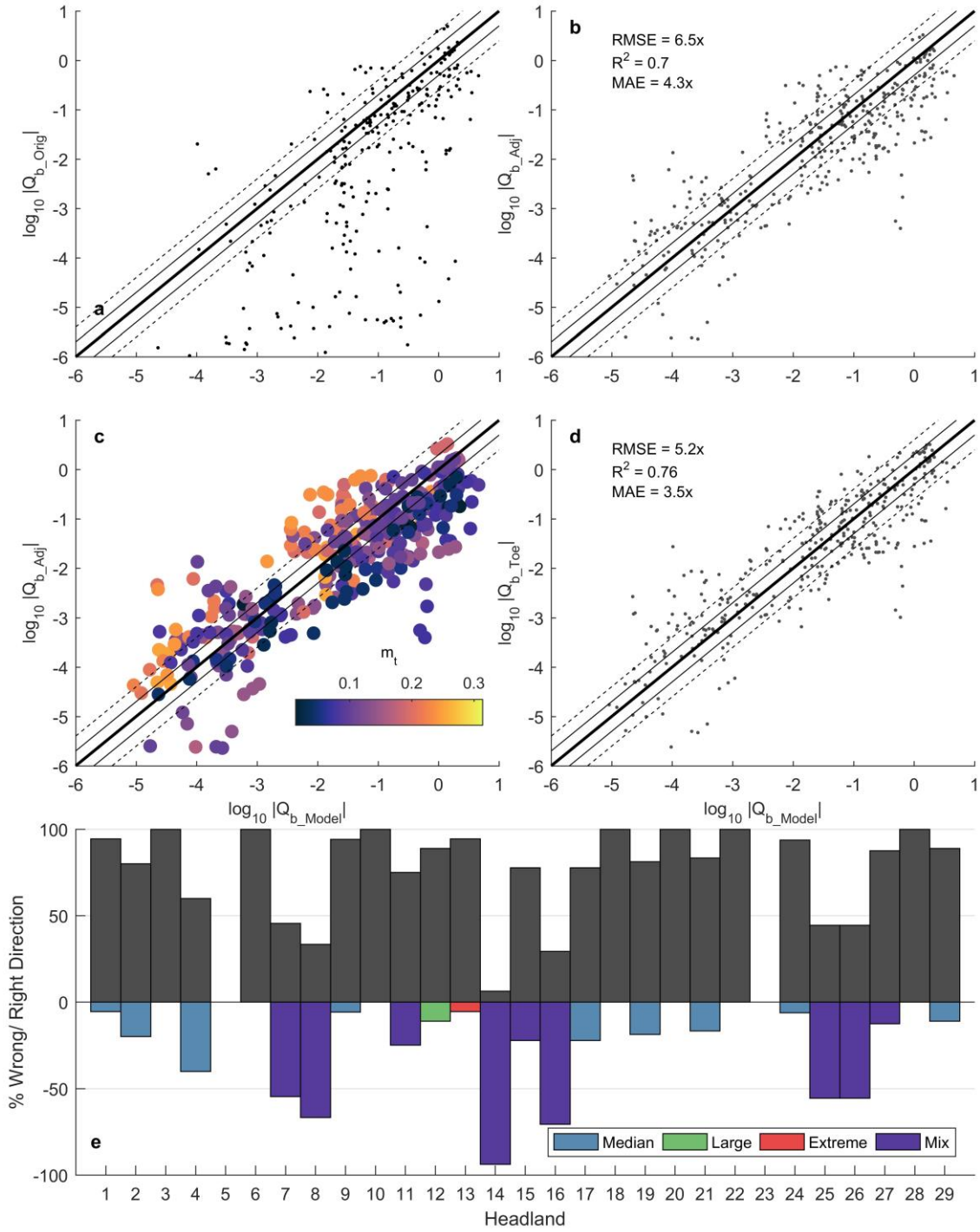

Figure 8: Comparison of headland bypassing parameterisations against the predictions of the Delft3D model. (a) The parameterisation taken directly from McCarroll et al. (In Review), without adjustment (Q_{b_Orig}), there are 135 outliers (N = 402) where Q_{b_Orig} predicted near zero bypassing. (b) The parameterisation of McCarroll et al. (In Review), adjusted to better fit these data (Q_{b_Adj}). Statistics are shown, calculated using the log-transformed data and converted into factor errors where relevant. The 1:1 line for a perfect model is shown in black (thick line), a factor 2 deviation from the perfect model is shown with thin black lines, and a factor 4 with dashed black lines. (c) The parameterisation as in (b) with colours representing the m_t parameter. (d) The parameterisation as in (b) with an additional term to account for variable depth off the headland toe via m_t (Q_{b_Toe}). (e) Percentage of scenarios where sand bypassing direction was correctly predicted (grey bars), or

incorrectly predicted (coloured bars). Colours represent the wave conditions where bypassing direction was wrongly predicted. No bars are shown where no bypassing occurred, and percentages were calculated relative to the number of cases where bypassing occurred.

488

489 4.2.3. The effect of spatially variable sediment distributions

490 The impact of introducing spatially variable sediments was determined for each headland using the
491 ratio:

$$\frac{\Delta Q_{b\_Sed}}{Q_{b\_Uni}} = \frac{Q_{b\_Sed} - Q_{b\_Uni}}{Q_{b\_Uni}}, \quad (7)$$

492 Where Q_{b_Sed} represents bypassing for the non-uniform sediment distribution scenarios, and Q_{b_Uni}
493 represents bypassing for the uniform sediment scenarios. Results are presented in Figure 9a. The main
494 impact of introducing a realistic sediment spatial distribution was that bypassing rates were generally
495 reduced, or bypassing ceased altogether (ratio = -1). There was only one headland (headland 6; Figure
496 9a) where bypassing direction was predicted to change (ratio < -1) between the uniform and spatially
497 variable sediment scenarios. This occurred for median waves and a low bypassing magnitude.

498 Eight headlands exhibited an activation of net bypassing in the case of non-uniformly distributed
499 sediment for at least one wave condition, and a further five exhibited an increase in net bypassing
500 rate, although this tended to be relatively small, never more than a factor 2 (ratio = 1). In these cases,
501 gross transport along the apex transect was greater for uniform sediments, however net bypassing in
502 was low or zero/ divergent. This was due to a relatively large magnitude divergent transport off the
503 headland toe in the uniform sediment scenario which opposed alongshore transport past the
504 headland further offshore, resulting in zero or low net bypassing for uniform sediment coverage. This
505 nearshore transport divergence was of a much lower magnitude when sediment was unavailable for
506 resuspension off the headland toe, and bypassing further offshore in the suspended load dominated
507 (example: headland 11 - Figure 9d, e).

508 Two conditions were determined that were indicative of where a sediment availability parameter
509 should be applied. Firstly, if $X_{head} < 1.5\ X_{surf}$ then bypassing was approximately equal to the uniform
510 sediment availability case and a sediment availability parameter need not be applied. Likewise, if
511 sediment is available off the headland toe (in this case tested at 100 m from the headland toe) then
512 bypassing can be approximated using the uniform sediment parameterisation and the sediment
513 parameter need not be applied. These conditions account for the headlands with zero or very small
514 relative change in Figure 9a.

For cases where these conditions indicate a change in bypassing rate due to sediment availability, a number of parameters were tested for influence on bypassing rates, including: cross-shore extent of sediment adjacent to the headland, sediment coverage ratio R_{sed}, X_{head}, Z_{toe}, headland alongshore length and headland perimeter length. No parameters indicated a clear correlation with changes in bypassing rates predicted by the model. A uniform reduction of an order of magnitude performed best when applied to Q_{b_Toe} (Equation 6).

$$Q_{b\_Sed} = 0.1 \times Q_{b\_Toe} \text{ for: } \frac{X_{head}}{X_{surf}} > 1.5 \ \& \text{ No sediment at headland toe,} \tag{8}$$

When applying the criteria discussed above with this parameter, the MAE for all headlands under the spatially variable sediment scenarios was reduced from a factor of 5.5 to a factor of 4.6 (Figure 9b, c). This indicates the parameters applied thus far are able to capture the order of magnitude of wave-forced instantaneous headland bypassing for different headland morphologies, at different tidal elevations, and for spatially variable sediments with an overall R^2 of 0.66. It remains to test the influence of tidal currents on bypassing rates.

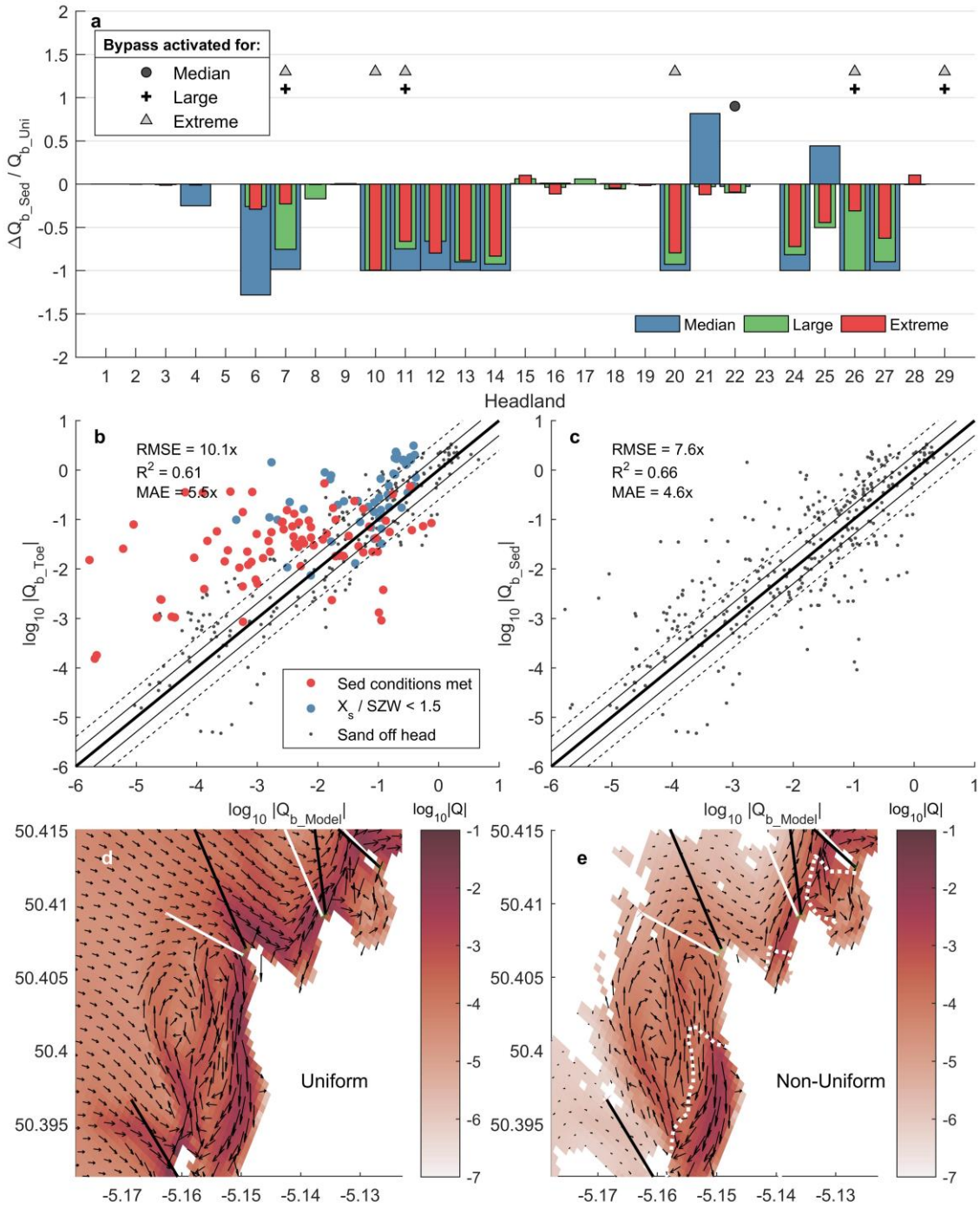

Figure 9: The effect of sediment availability of sand bypassing rates, and comparisons of headland bypassing parameterisations against the predictions of the Delft3D model. (a) The difference between bypassing rates for limited versus uniform sediment availability ($\Delta Q_{b\_Sed} = Q_{b\_Sed} - Q_{b\_Uni}$), relative to the magnitude of bypassing for uniform sediments (Q_{b_Uni}), for each headland. Bars are coloured for each wave condition. Bar values were averaged over all wave directions. Symbols indicate wave conditions where net bypassing was activated in Q_{b_Sed} but not in Q_{b_Uni} for at least one wave direction. (b) The parameterisation Q_{b_Toe} versus the Delft3D model. Statistics are shown, calculated using the log-transformed data and converted into factor errors where relevant. Colours indicate data where sediment was absent from the headland toe. Blue data indicate cases where $X_{head} / X_{surf} < 1.5$. (c) The parameterisation of (b) with an added term to account for limited sediment

availability. (d, e) Example headland (11 - Kelsey Head) where net bypassing was divergent for uniform sediments but upcoast for non-uniform sediments, with sand transport magnitude and vectors shown. Colours and vectors are log-scaled. The condition shown is extreme waves from 292.5° at SHW. Dashed white lines in (e) indicate the offshore limit of sand coverage.

4.2.4. Tidal currents and wave-current interactions

The scenarios described above were repeated with the inclusion of tidal currents. Tidal currents at the times of SHW and SLW extracted for processing ranged between 0.02 and 1 ms^{-1} in magnitude off the headland apexes, with greater magnitude off larger promontories. Whilst these were not the peak ebb and flood currents, they represent a large range of velocities for the assessment of the impact of tidal currents on instantaneous bypass rates. Bypass rates were averaged over all times of SHW or SLW respectively. Example results are presented in Figure 10 (a-d) for the modal wave direction (281.25°) and at SLW (when bypassing rates tended to be larger). The same figure showing bypassing at SHW is provided in supplementary Figure FS1.

Tidally-driven bypassing, in the absence of wave forcing, had a maximum magnitude of ca. 10^{-3} m^3s^{-1} across SHW and SLW in the case of uniform sediments (Figure 10a-b). The greatest bypassing magnitude for uniform sediments was off Trevose Head (headland 23), the largest promontory in the domain. Tide-driven bypassing directions sometimes opposed the wave-driven bypassing. In this case, for median waves (Figure 10a), bypassing under combined wave-tide forcing tended to follow the tide-driven bypassing direction, indicating that median waves act to enhance sand transport in the tidal direction. For extreme waves (Figure 10b), bypassing direction rarely changed between wave-only and wave-tide scenarios (headland 15 at SHW only), and there was generally only a minor enhancement of bypassing magnitudes relative to wave-only scenarios. In some cases (headlands 20 (SHW) and 26) bypassing was switched off with the addition of tidal forcing.

Tide-driven bypassing was greatly reduced when non-uniform sediment distributions were included (Figure 10c-d). Bypassing was switched off across most headlands, and only active for seven headlands in total between SHW and SLW (1, 2, 10, 14, 21, 23 & 27). In these cases, bypassing was generally downcoast (with the exception of 10 and 21 at SLW) and of very low magnitude. The greatest magnitude was for headlands 1 and 2 at SHW, which indicated tidally driven sand transport out of St Ives Bay to the west, in agreement with transport directions reported in King et al., (2019a). Regardless of low tide-only bypassing rates, tidal currents were able to induce reversals in the median wave bypassing directions (Figure 10c) indicating that wave-current interactions are important during median waves, even when tide-only bypassing may be negligible.

This is indicated in the relative change bar plots for uniform sediments (Figure 10e) and non-uniform sediments (Figure 10f). Here, relative differences were averaged over the SHW and SLW scenarios and all wave directions. The largest relative differences tended to be for median waves (blue bars). There was also a widespread activation of bypassing under the wave-tide forcing when wave-only bypassing was nil, particularly for median and large waves.

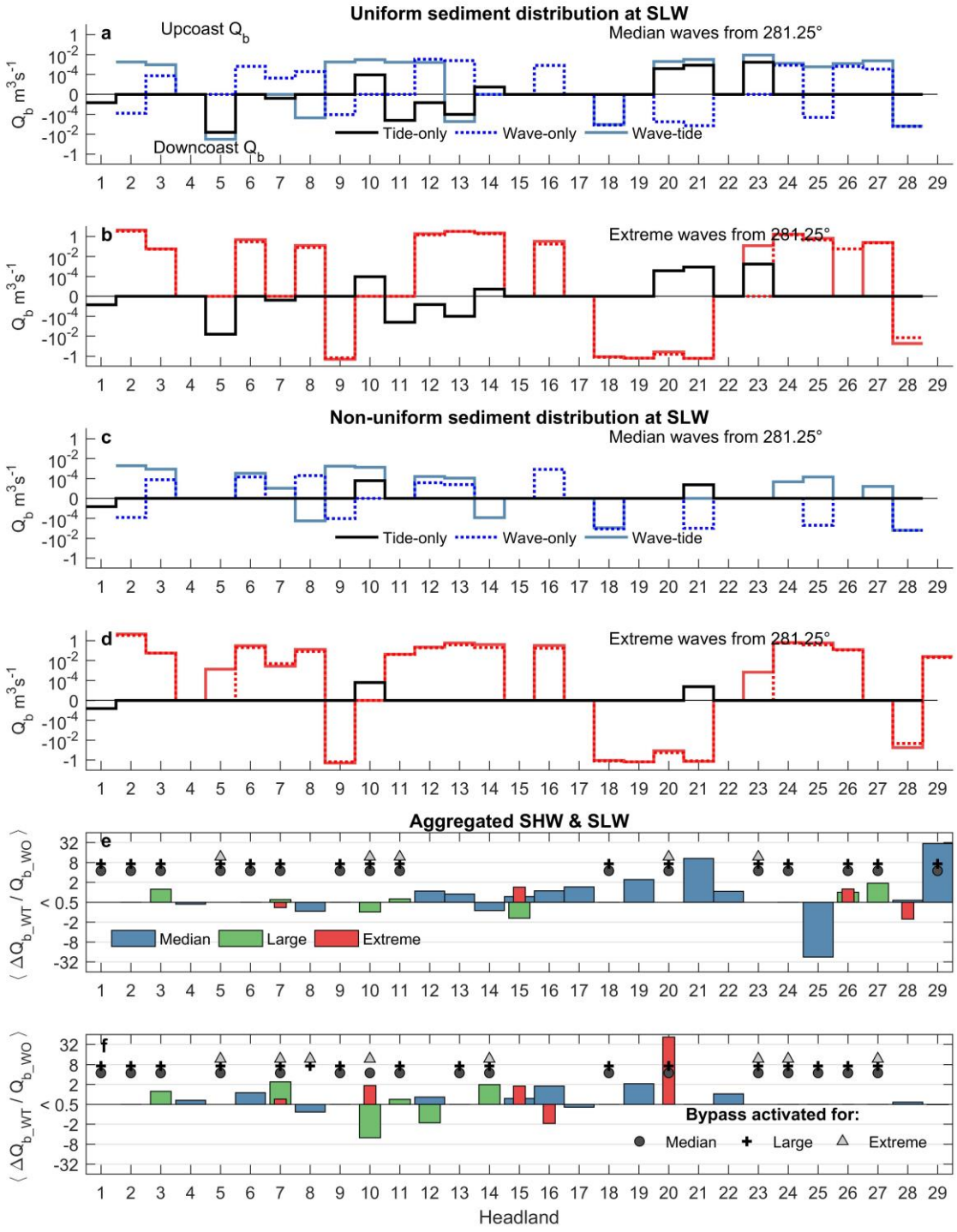

Figure 10: Comparison between tide-only, wave-only and wave-tide bypassing rates, for waves from the modal wave direction 281.25°. Instantaneous bypassing rates are presented for median and

extreme waves for uniform sediments (a, b respectively) and non-uniform sediments (c, d respectively) for tide-only (black solid line), wave-only (coloured solid line) and wave-tide (coloured dashed line). Positive values represent upcoast bypassing, and downcoast bypassing for negative values. Values are for each headland. (e, f) Relative differences for uniform sediments (e) and non-uniform sediments (f) per headland. Values are an average over all water levels and wave directions. Bars are coloured for each wave condition. Symbols indicate wave conditions where bypassing was activated by wave-tide forcing Q_{b_WT} but not by wave only forcing Q_{b_WO} for at least one condition. The y-scale increases in $\log_2$ increments.

To quantify the relative impact of waves, tides and their non-linear interactions, bypassing rates were used to determine their wave-tide dominance classification as per King et al., (2019a). This indicates whether the dominant driver of sand transport is tidal forcing (T), wave forcing (W) or the non-linear interactions between the waves and tides (N) using two ratios:

$$R1 = T : (W + N), \tag{9}$$

$$R2 = W : N, \tag{10}$$

Where *W* represents wave-only bypassing rate, *T* represents tide-only bypassing rate and *N* represents the contribution of non-linear wave-current interactions to bypassing, calculated as:

$$N = WT - (W + T), \tag{11}$$

Where *WT* is the bypass rate under coupled wave-tide forcing. Results of the classification over all scenarios are presented in Figure 11. Lower-case letters indicate a sub-dominant contribution from the denoted forcing mechanism. There was no appreciable difference between wave directions, therefore all directions were aggregated to calculate the percentage of data in each class for each scenario wave scenario (columns) and waver level (rows). Median waves exhibit non-linear wave-tide interaction dominance of bypassing rates under all scenarios for the majority of headlands. At SLW around 10% of headlands shift from non-linear dominated to wave dominated under median waves, reflecting greater wave impacts at low water. The relative influence of tides under these waves is greatest at SHW, mainly manifested as a subdominant tidal contribution, denoted by a lower-case “t” (e.g. Nt). This reduces to < 5 % of data at SLW.

Dominant forcing shifts towards wave-dominance as the wave exceedance increases (median → large → extreme). For large and extreme waves, the majority of bypassing is wave-dominated in this macrotidal environment at both SHW and SLW. For these waves and uniform sediments there is a secondary, tide dominated mode of sand transport for ~ 18 % of data at SLW (Figure 11 e – f). This occurs where wave-only bypassing was weak or negligible, for example at headland 23. This signal is

much reduced, or negligible, for non-uniform sediment distributions (Figure 11 g – l), reflecting the much reduced tidally driven bypassing when sediment is not available off large headland promontories. For extreme waves and non-uniform sediments (Figure 11i, l), wave-current interactions have a greatest impact at SLW, shifting the class of bypassing from W to Wn for around 30 % of the data.

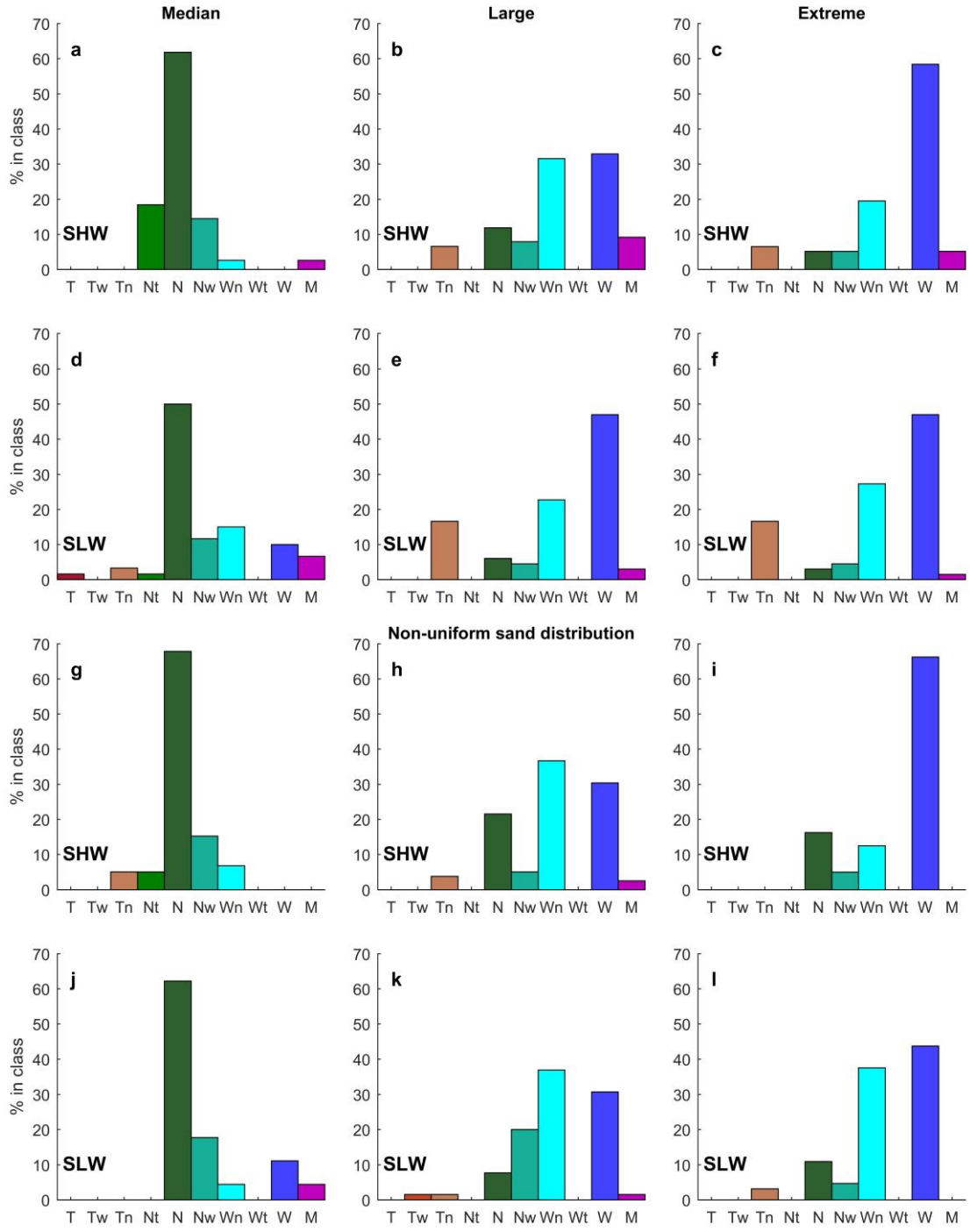

Figure 11: Wave-tide dominance classification as per King et al. (2019a). Classifications range from tide-dominate ("T" – red) through dominance of non-linear wave-tide interactions ("N" – green) to

wave dominated ("W" – blue), and mixed ("M" – purple). Lower-case letters denote a subdominant contribution from the denoted process. Data for all three wave directions were aggregated into median (50% exceedance, column 1), large (5% exceedance) and extreme (12h exceedance) wave conditions for simplicity. Classifications are shown for uniform (a – f) and non-uniform (g – l) sediment distribution. Water levels are denoted by SHW and SLW for spring high and low water respectfully.

588

589 # 5. Discussion

590 This paper tested the influence of wave, tide and morphological controls on instantaneous headland
591 sand bypassing using a coupled wave-tide numerical model, and tested the performance of an existing
592 parameterisation when applied to realistic headland morphologies and sediment coverage, making
593 recommendations for additional terms to improve model performance. We discuss connectivity
594 between embayments via headland bypassing along this stretch of coast in the context of previous
595 work in this region and globally (Section 5.1). We then discuss the assumptions and limitations of the
596 proposed bypassing parameterisation (Section 5.2), before outlining practical considerations for the
597 application of a headland bypassing parameter with recommendations for further research (Section
598 5.3).

599 ## 5.1. Headland bypassing on embayed coastlines

600 Prior studies on headland bypassing that consider wave and tidal forcing have established that
601 bypassing is generally a wave-dominated process (George et al., 2019; McCarroll et al., 2018; Valiente
602 et al., 2020; Vieira da Silva et al., 2018); however, the non-linear effects between waves and tidal
603 forcing have not been fully quantified yet, although McCarroll et al. (2018) do compare bypassing
604 between spring and neap tide conditions. Results presented here suggest that, in macrotidal
605 environments, bypassing during energetic events (deep water $H_s \geq 6$ m) is wave-dominated; however,
606 during median wave events (deep water $H_s = 2$ m) bypassing rates are dominated by non-linear wave-
607 current interactions between waves and tidal velocities, with waves enhancing bypassing in the tidal
608 direction and activation of sand transport when tide-only bypassing is negligible.

609 Non-uniform sediment availability reduces tide-only bypassing when sand is not available adjacent to
610 the headland apex, where tidal currents are amplified (King et al., 2019a). Bypassing in these situations
611 was in the suspended load. Tides have a greatest impact for median waves: tidal elevations modulate
612 bypassing by a factor of 4 between SHW and SLW because of modulation of headland cross-shore
613 length, whilst the impact of currents is generally not more than a factor of 2 for non-uniform sand
614 coverage, matching the minor tidal control reported by Valiente et al. (2020). The primary control on
615 bypassing rates is the cross-shore length of the headland relative to surf zone width, and low bypassing
616 rates for $X_{head} / X_{surf} > 3$ matches McCarroll et al. (In Review).

Reduced depth off the headland toe increases headland bypassing rates following the relationship in Equation 6. McCarroll et al. (In Review) report an increase in bypassing magnitude of a factor 1.5 for headlands with sub-aqueous ridges of around 1 to 3 m prominence, resulting from increased orbital velocities at the bed off the headland. Equation 6 predicts this, as a decrease in depth off the headland toe of ca. 2 m for depths between 3 and 10 m results in an increase in bypassing of a factor between 1.3 and 1.8. This acts as an additional term to the parameterisation (Equations 5 & 6).

The parameterisation of the form of Equations 1 and 5 had previously been shown to apply for an isolated headland with uniform offshore bathymetry, sediments and wave-only forcing (McCarroll et al., In Review). The alteration of the exponent between Equations 1 and 5 reduces the rate of decay of the bypassing parameter as headlands extend beyond the surf zone (X_{heas} / X_{surf} > 1). This implies, for realistic headland morphologies and bathymetric expressions, headland bypassing occurs for greater relative headland cross-shore extents than predicted through idealised scenarios with a linear shoreface gradient.

We show that with this minor adaptation, and the addition of terms for variable headland toe depth (Equation 6) and sediment availability (Equation 8), instantaneous headland bypassing is amenable to parameterisation along stretches of coastline with realistic morphologies and spatial variability in sand coverage. The final parameterisation is where $X_{head} > 1.5\ X_{surf}$ and there is no sand at the headland toe is:

$$Q_{b\_Sed} = 0.1 \times Q_0 \cdot e^{-\left(\frac{X_{head}}{X_{surf}}\right)^{0.5}} \cdot e^{3.5-\frac{1}{(m_t-0.7)^2}}, \quad (12)$$

Else if $X_{head} \leq 1.5\ X_{surf}$ or there is sand at the headland toe:

$$Q_{b\_Sed} = Q_0 \cdot e^{-\left(\frac{X_{head}}{X_{surf}}\right)^{0.5}} \cdot e^{3.5-\frac{1}{(m_t-0.7)^2}}, \quad (13)$$

Where Q_0 is the uninhibited longshore transport formulation of van Rijn (2014):

$$Q_0 = 0.00018 \cdot K \cdot g^{0.5} \cdot \tan(\beta)^{0.4} \cdot D_{50}^{-0.6} \cdot H_{s,b}^{3.1} \cdot \sin(2\alpha_b), \quad (14)$$

This parameterisation is able to reproduce modelled bypassing rates with a MAE of a factor of 4.4, which suggests it is possible to predict the magnitude of instantaneous bypassing rates with some confidence and accuracy.

Bypassing directions were mainly predicted correctly using the breaking wave angle relative to shore normal, but with exceptions. Of all cases, 23 % of directions were predicted wrongly, of which 43 %

were for median wave, low bypassing conditions, and the remainder were associated mostly with six headlands. These cases were associated with bypassing offshore in the opposite direction to the prediction and either divergent transport nearshore of the headland apex, or opposing bypassing nearshore in the predicted direction. Offshore transport was driven by strong embayment cellular circulation and deflection rips from the downwave headland driving alongshore flow offshore past the upwave headland (e.g. headland 14), or activation of sand transport off the headland apex where sand was available at the headland toe (e.g. headland 7).

Valiente et al. (2019b) suggested the concept of a 'river of sand' linking embayments along this stretch of coast through headland bypassing, based on observations of inter- and sub-tidal volumetric changes in response to environmental forcing at Perranporth. Bypassing magnitude and directions at Perranporth (headland 9) and the adjacent bays (headlands 7 - 11) match predictions published previously, with northward bypassing during median wave conditions and southward bypassing for energetic wave forcing at Perranporth (McCarroll et al., 2018; Valiente et al., 2020). This lends confidence to the predictions of this model. Results presented here indicate widespread linkages between the embayments along this coastline, with only two headlands (5 - Godrevy Point & 23 - Trevose Head) predominantly blocking longshore sand transport. This suggests that headland bypassing has the potential to be ubiquitous along exposed embayed coastlines globally.

5.2. Assumptions and limitations

The parameterisation terms presented in Equations 2, 5, 6, and 8 have been tested against a wide range of headland and bay morphologies, wave forcing conditions and tidal elevations. This parameterisation accurately predicts instantaneous bypassing magnitude in wave-dominated conditions. This study considers instantaneous bypassing rates, without considering morphology change and limited sediment depth. Whilst we do not consider different grain sizes here, grain size is accounted for in Equation 2, and its effects on bypassing rates are covered by McCarroll et al. (In Review).

Morphology was kept constant to avoid feedback effects over the course of a simulation, keeping bed morphology constant and not considering limited sediment depth, enabling averaging over time under consistent forcing conditions for analysis. This enabled a constant morphology to be quantified and morphological controls such as headland toe depth to be determined. Thus, the results presented here do not account for cases where strong beach rotation drives accumulation of sediment against the downwave headland and driving bypassing (Wiggins et al., 2019), or where limited sediment depth constrains potential bypassing magnitude. Thus, results presented here might be considered an upper limit for a given bed morphology and spatial sediment coverage.

The parameterisation does not account for tidal currents and their interactions with waves, or wind driven currents. Vieira da Silva et al. (2018) found that waves drove sand bypassing at a rate two orders of magnitude greater than wind-driven currents. Our results suggest that bypassing is wave-dominated during energetic events, even in a macrotidal environment; however, wave-current interactions are dominant for median wave conditions. Thus, we recommend caution when applying the parameter for median waves in macrotidal environments as wave-current interactions can be dominant. The parameterisation accounts for varying tidal elevation through changes to the apparent headland morphology (changes to X_{head} and Z_{toe}).

There is a scarcity of observations of headland bypassing rates. Observations during low energy conditions have been made by tracer experiment (Duarte et al., 2014) and sand trapping (Vieira da Silva et al., 2016). In other cases, volumetric changes have been used to infer bypassing (Klein et al., 2010; McCarroll et al., 2019; Valiente et al., 2019b; Wiggins et al., 2019). Thus, bypassing rates presented here could not be validated directly, and validation relied upon validation of current velocities, including near-bed velocities, and comparison of bypassing magnitudes to those reported elsewhere using different models (McCarroll et al., 2018, In Review; Valiente et al., 2020), whilst using transport formulae and settings used elsewhere under similar conditions (King et al., 2019a; Luijendijk et al., 2017; McCarroll et al., 2018; van Rijn, 2007a, b). Thus, absolute bypassing magnitudes presented here should be considered exploratory in nature.

5.3. Practical considerations for coastal managers

In applying the parameterisation presented in this paper, we summarise some considerations to be taken into account.

1. Morphology:
    a. For pocket beaches where it is difficult to determine the beach orientation, or beach orientation is highly oblique to the orientation of the adjacent coastlines up and downcoast, it is recommended to take the orientation of the nearest adjacent stretch of open beach or the general orientation of the coastline.
    b. Headland transects and morphology should be determined as described in McCarroll et al. (In Review; their section 5) with the addition of toe depth along the apex transect (50 m from the headland toe) as shown in Figure 5.
    c. It should be determined if sediment is present at the headland toe, for example from high-resolution bathymetry using the method described in Section 3.2.1 (Figure 2).

d. Repeat the process for beaches adjacent on the up- and downcoast headland aspects, giving an upcoast and downcoast morphology (Figure 5).

2. Wave forcing:
    a. A method for transformation of waves from offshore to the breakpoint is presented in McCarroll et al., (In Review) using linear wave theory and van Rijn (2014).
3. Unconstrained longshore flux:
    a. An estimate of unconstrained flux alongshore Q_0, can be determined using van Rijn (2014); Equation 2/ 14.
4. Wave-forced bypassing estimation:
    a. Using Equations 12/ 13, an estimation of wave forced bypassing can be determined for a given stretch of coast. These should be applied baring the following points in mind:
    b. For $X_{head} < 0.5\ X_{surf}$, the unconstrained longshore flux should be applied (Equation 2/ 14), and the headland assumed to not block bypassing;
    c. For $X_{head} > 5\ X_{surf}$, bypassing can be assumed to be very low or negligible;
    d. Equation 13 applies to all other cases, determining the reduction in longshore flux due to the headland;
    e. Equation 12 applies instead of Equation 13 only when sediment is not available off the headland apex, and $X_{head} > 1.5\ X_{surf}$.

In macrotidal environments and low wave energy, it may be prudent to assess the dominant transport mode to check the applicability of this parameter. The parameter may underestimate transport or predict bypassing in the wrong direction where wave-current interactions are important. This tended to be for low wave energy and spring tides in this macrotidal environment (King et al., 2019a). Variable sediment depth is not accounted for in this parameter, as discussed in Section 5.2. Understanding the role of spatially variable sediment depth in constraining headland bypassing rates needs to be addressed through further research. In this context, these results and this parameter may represent an upper estimate of potential bypassing rates.

To constrain the applicability of this parameter in cases where bypassing could be dominated by wave-current interactions, a means of determining the dominant sand transport mode under specific wave and tide conditions without a computationally expensive numerical model could be of benefit. This would be an application and extension of the classification scheme of King et al., (2019a). Preliminary work on this shows promising potential for the prediction of wave-tide dominance of sand transport based on readily available predictors such as tide range, maximum current speed, significant wave height, peak period, direction and depth (King et al., 2019b).

6. Conclusions

- A validated 3D numerical model (Delft3D) was developed for a 75 km stretch of macrotidal, exposed coastline to investigate environmental and morphological controls on headland sand bypassing. Three wave exceedance conditions were tested (50 %, 5 % and 12 hour) from three directions, with both uniform and variable sediments, with and without tidal currents.
- Headland morphology was generally asymmetric, suggesting a predisposition to bypassing towards the northeast along the North Coast of Cornwall.
- Bypassing is strongly dependent upon headland cross-shore extent relative to surf zone width. When cross-shore length exceeds five surf zone widths, bypassing is effectively negligible.
- Headland toe depth represents an important secondary control on bypassing magnitude, through moderation of wave impacts off the headland toe.
- Sediment spatial variability can reduce bypassing by several orders of magnitude depending on the relative coverage of sand adjacent to the headland, and reduces the effect of tidal currents relative to a uniform sand bed.
- Tidal elevations are a secondary control on bypassing during energetic wave events, and have a greater relative impact during median wave energy conditions. The impact of tidal elevations is largely through modifications of the apparent morphology of the headland and in this macrotidal environment modulates bypassing rates by a factor of 4 on average for median wave energy, and a roughly factor 2 for energetic waves.
- Tidal currents have a minor effect during energetic waves, however they have a greater impact for median wave energy conditions through non-linear wave tide interactions. Wave-current interactions can dominate bypassing during median wave energy conditions at spring tides.
- An existing parameterisation based on an isolated headland with uniform offshore bathymetry was tested against bypassing with realistic embayment morphologies, and additional terms for headland toe depth and sediment availability were explored.
- Bypassing rates were predicted with mean absolute error of a factor 4.4. Generalised estimations of bypassing in realistic settings are entirely novel, therefore any predictor within an order of magnitude is highly useful. These results indicate wave-dominated bypassing is amenable to parameterisation in embayed settings.

7. Acknowledgements

We acknowledge the UK Hydrographic Office for the VORF corrections and single-beam bathymetry. High-resolution bathymetry here contains public sector information, licensed under the Open Government Licence v3.0, from the Maritime and Coastguard Association. We acknowledge the MET Office (Andy Saulter) for the hydrodynamic and wave forcing data and NOAA for the atmospheric pressure and wind data, and EMODnet bathymetry Consortium for the EMODnet Digital Bathymetry (DTM 2016). This research was supported by the NERC-funded BLUECoast Project (NE/N015525/1). The data on which this paper is based are publicly available from the corresponding author and will be made available online via the University of Plymouth PEARL open access research repository upon publication.

8. References

Ab Razak, M. S., Dastgheib, A. & Roelvink, D. (2013). Sand bypassing and shoreline evolution near coastal structure, comparing analytical solution and XBeach numerical modelling. *Journal of Coastal Research*, 65, 2083 – 2088.

Acworth, C. & Lawson, S. (2012). The Tweed River entrance sand bypassing project, ten years of managing operations in a highly variable coastal system. *Proceeding of the 20th NSW Coastal Conference 2012 Tweed Head*, 1 – 23.

Akan, C., McWilliams, J. C. & Uchiyama, Y. (2020). Topographic and coastline influences on surf Eddies. *Ocean Modelling*, 147, 101565. https://doi.org/10.1016/j.ocemod.2019.101565

Bentamy, A., & Fillon, D. C. (2012). Gridded surface wind fields from Metop/ASCAT measurements. International Journal of Remote Sensing, 33(6), 1729 – 1754. https://doi.org/10.1080/01431161.2011.600348

Booij, N., Holthuijsen, L. H., & Ris, R. C. (1999). A third-generation wave model for coastal regions 1. Model description and validation. *Journal of Geophysical Research*, 104(C4), 7649 – 7666. https://doi.org/10.1029/98JC02622

Bricheno, L. M., Wolf, J., & Aldridge, J. (2015). Distribution of natural disturbance due to wave and tidal bed currents around the UK. *Continental Shelf Research*, 109, 67– 77. https://doi.org/10.1016/j.csr.2015.09.013

Burrough, P. A. (1981). Fractal dimensions of landscapes and other environmental data. *Nature*, **294**, 240 – 241.

Castelle, B. & Coco, G. (2012). The morphodynamics of rip channels on embayed beaches. *Continental Shelf Research*, 43, 10 – 23. https://doi.org/10.1016/j.csr.2012.04.010

Castelle, B. & Coco, G. (2013). Surf zone flushing on embayed beaches. *Geophysical Research Letters*, 40, 2206 – 2210. https://doi.org/10.1002/grl.50485

Castelle, B., Scott, T., Brander, R. W. & McCarroll, R. J. (2016). Rip current types, circulation and hazard. *Earth-Science Reviews*, 163, 1 – 21.

Castelle, B., Dodet, G., Masselink, G., & Scott, T. (2018). Increased winter-mean wave height, variability and periodicity in the North-East Atlantic over 1949–2017. *Geophysical Research Letters*, 45, 3586 – 3596. https://doi.org/10.1002/2017GL076884

Collins, M. B. (1987). Sediment transport in the Bristol Channel: A review. Proceedings of the Geologists' Association, 98(4), 367 – 383. https://doi.org/10.1016/S0016-7878(87)80076-7

Davidson, M. A., Lewis, R. P. & Turner, I. L. (2010). Forecasting seasonal to multi-year shoreline change. *Coastal Engineering*, 57, 620–629.

Draper, L. (1967). Wave activity at the sea bed around northwestern Europe. *Marine Geology*, 5(2), 133 – 140. https://doi.org/10.1016/0025-3227(67)90075-8

Duarte, J., Taborda, R., Ribeiro, M., Cascalho, J., Silva, A. & Bosnic, I. (2014). Evidences of sediment bypassing at Nazaré headland revealed by a large scale sand tracer experiment. *Proceedings of the 3rd as Jornadas de Engenharia Hidrográica*, Lisboa, Portugal, 24–26 June 2014, 289 – 292.

EMODnet Bathymetry Consortium. (2016). EMODnet Digital Bathymetry (DTM 2016). EMODnet Bathymetry Consortium. https://doi.org/10.12770/c7b53704-999d-4721-b1a3-04ec60c87238

Evans, O. F. (1943). The relation of the action of waves and currents on headlands to the control of shore erosion by groins. *Proceedings of the Oklahoma Academy of Sciences*, 24, 9 – 13.

Fellowes, T. E., Villa-Concejo, A. & Gallop, S. L. (2019). Morphometric classification of swell-dominated embayed beaches. *Marine Geology*, 411, 78 – 87. https://doi.org/10.1016/j.margeo.2019.02.004

Fitzgerald, D. M., Kraus, N. C. & Hands, E. B. (2000). Natural Mechanisms of Sediment Bypassing at Tidal Inlets. CHETN-IV-30. U.S. Army Corps of Engineers, Vicksburg, MS. https://apps.dtic.mil/dtic/tr/fulltext/u2/a588774.pdf

Fredsøe, J. (1984). Turbulent boundary layer in wave-current motion. *Journal of Hydraulic Engineering*, 110(8), 1103 – 1120. https://doi.org/10.1061/(ASCE)0733-9429(1984)110:8(1103

Genest, C. & Favre, A. C. (2007). Everything you always wanted to know about copula modeling but were afraid to ask. *Journal of Hydrologic Engineering*. 12(4), 347 – 368. https://doi.org/10.1061/(ASCE)1084-0699(2007)12:4(347)

George, D. A., Largier, J. L., Storlazzi, C. D. & Barnard, P. L. (2015). Classification of rocky headlands in California with relevance to littoral cell boundary delineation. *Marine Geology*, 369, 137 – 152.

George, D. A., Largier, J. L., Pasternack, G. B., Barnard, P. L., Storlazzi, C. D. & Erikson, L. H. (2019). Modelling sediment bypassing around idealized rocky headlands. *Journal of Marine Science and Engineering*, 7(40). https://doi.org/10.3390/jmse7020040

Goodwin, I. D., Freeman, R., Blackmore, K. (2013). An insight into headland sand bypassing and wave climate variability from shoreface bathymetric change at Byron Bay, New South Wales, Australia. Marine Geology, 341, 29 – 45. https://doi.org/10.1016/j.margeo.2013.05.005

Grunnet, N. M., Walstra, D. J. R. & Ruessink, B. G. (2004). Process-based modelling of a shoreface nourishment. *Coastal Engineering*, 51, 581–607. https://doi.org/10.1016/j.coastaleng.2004.07.016

Holt, J. T., James, I. D., & Jones, E. J. (2001). An s coordinate density evolving model of the northwest European continental shelf: 2. Seasonal currents and tides. *Journal of Geophysical Research*, 106(C7), 14,035– 14,053. https://doi.org/10.1029/2000JC000303

King, E. V., Conley, D. C., Masselink, G., Leonardi, N., McCarroll, R. J., & Scott, T. (2019a). The impact of waves and tides on residual sand transport on a sediment-poor, energetic, and macrotidal continental shelf. *Journal of Geophysical Research: Oceans*, 124, 4974 – 5002. https://doi.org/10.1029/2018JC014861

Klein, A.H.F.; Ferreira, Ó.; Dias, J.M.A.; Tessler, M.G.; Silveira, L.F.; Benedet, L.; de Menezes, J.T.; de Abreu, J.G.N. Morphodynamics of structurally controlled headland-bay beaches in southeastern Brazil: A review. *Coastal Engineering*, 2010, 57, 98–111.

Komen, G., Hasselmann S. & Hasselmann, K. (1984). On the existence of a fully developed wind-sea spectrum. *Journal of Physical Oceanography*, 14, 1271 – 1285.

Lesser, G. R., Roelvink, J. A., Van Kester, J. A. T. M., & Stelling, G. S. (2004). Development and validation of a three-dimensional morphological model. *Coastal Engineering*, 51(8-9), 883 – 915. https://doi.org/10.1016/j.coastaleng.2004.07.014

Luijendijk, A. P., Ranasinghe, R., de Schipper, M. A., Huisman, B. A., Swinkels, C. M., Walstra, D. J. R. & Stive, M. J. F. (2017). The initial morphological response of the Sand Engine: A process-based modelling study, *Coastal Engineering*, 119, 1 – 14. https://doi.org/10.1016/j.coastaleng.2016.09.005

Madsen, O., Poon Y. K. & Graber, H. (1988). Spectral wave attenuation by bottom friction: Theory. *Proceedings 21th International Conference Coastal Engineering*, ASCE, 492 – 504.

McCarroll, R. J., Brander, R. W., Turner, I. L. & Van Leeuwen, B. (2016). Shoreface storm morphodynamics and mega-rip evolution at an embayed beach: Bondi Beach, NSW, Australia. *Continental Shelf Research*, 116, 74 – 88. https://doi.org/10.1016/j.csr.2016.01.013

McCarroll, R. J., Masselink, G., Valiente, N. G., Scott, T., King, E. V. & Conley, D. (2018). Wave and Tidal Controls on Embayment Circulation and Headland Bypassing for an Exposed, Macrotidal Site. Journal of Marine Science and Engineering, 6(3), 94. https://doi.org/10.3390/jmse6030094

McCarroll, R. J., Masselink, G., Wiggins, M., Scott, T., Billson, O., Conley, D. C. & Valiente, N. G. (2019). High-efficiency gravel longshore sediment transport and headland bypassing over an extreme wave event. *Earth Surface Processes and Landforms*, 44, 2720 – 2727. https://doi.org/10.1002/esp.4692

McCarroll, R. J., Masselink, G., Valiente, N. G., King, E. V. Scott, T., Stokes, C. & Wiggins, M. (In Review). A general expression for wave-induced sediment bypassing of an isolated headland. *Coastal Engineering*. Pre-print: https://osf.io/preprints/eartharxiv/67rhx/download

McConnell, N., King, R., Tonani, M., O'Dea, E., Martin, M., Sykes, P. & Ryan, A. (2017). North West European Shelf Production Centre NORTHWESTSHELF_ANALYSIS_FORECAST_PHYS_004_001_b. Quality Information Document. Issue 3.5. Copernicus Marine Environment Monitoring Service.

Mouragues, A., Bonneton, P., Castelle, B., Marieu, V., McCarroll, R. J., Rodriguez-Padilla, I., Scott, T. & Sous, D. (2020). High-energy surf zone currents and headland rips at a geologically constrained mesotidal beach. *Journal of Geophysical Research: Oceans*, 125, e2020JC016259. https://doi.org/10.1029/2020JC016259

O'Dea, E. J., Arnold, A. K., Edwards, K. P., Furner, R., Hyder, P., Martin, M. J., Siddorn, J. R., Storkey, D., While, J., Holt, J. T., & Liu, H. (2012). An operational ocean forecast system incorporating NEMO and SST data assimilation for the tidally driven European North-West shelf. Journal of Operational Oceanography, 5(1), 3 – 17. https://doi.org/10.1080/1755876X.2012.11020128

Pingree, R. D., & Griffiths, D. K. (1979). Sand transport paths around the British Isles resulting from M2 and M4 tidal interactions. *Journal of the Marine Biological Association of the United Kingdom*, 59(2), 497– 513. https://doi.org/10.1017/S0025315400042806

Prodger, S., Russell, P., Davidson, M., Miles, J. & Scott, T. (2016). Understanding and predicting the temporal variability of sediment grain size characteristics on high-energy beaches. *Marine Geology*, **376**, 109 – 117.

Prodger, S., Russell, P., & Davidson, M. (2017). Grain-size distributions on high-energy sandy beaches and their relation to wave dissipation. *Sedimentology*, 64(5), 1289 – 1302. https://doi.org/10.1111/sed.12353

Ribeiro, M. S. A. (2017). *Headland sediment bypassing processes* (Doctoral dissertation). University of Lisbon. 229 p. https://pdfs.semanticscholar.org/e6be/c734b7b57592213848201567a80e1157d2b7.pdf

Saha, S., Moorthi, S., Wu, X., Wang, J., Nadiga, S., Tripp, P., Behringer, D., Hou, Y. T., Chuang, H. Y., Iredell, M., Ek, M., Meng, J., Yang, R., Mendez, M. P., van den Dool, H., Zhang, Q., Wang, W., Chen, M., & Becker, E. (2014). The NCEP Climate Forecast System version 2. *Journal of Climate*, 27(6), 2185 – 2208. https://doi.org/10.1175/JCLI-D-12-00823.1

Saulter, A. (2017). North West European Shelf Production Centre: NORTHWESTSHELF_ANALYSIS_FORECAST_WAV_004_012. Quality Information Document. Issue 1.0. Copernicus Marine Environment Monitoring Service.

Scott, T., Austin, M., Masselink, G. & Russell, P. (2016a). Dynamics of rip currents associated with groynes — Field measurements, modelling and implications for beach safety. *Coastal Engineering*, 107, 53 – 69.

Scott, T., Masselink, G., O'Hare, T., Saulter, A., Poate, T., Russell, P., Davidson, M. & Conley, D. (2016b). The extreme 2013/2014 winter storms: Beach recovery along the southwest coast of England. *Marine Geology,* 382, 224 – 241.

937 Short, A. D. (1985). Rip-current type, spacing and persistence, Narrabeen Beach, Australia. *Marine*
938 *Geology*, 65(1 – 2), 47 – 71.
939 https://doi.org/10.1016/0025-3227(85)90046-5

940 Short, A. D. & Masselink, G. (1999). Structurally Controlled Beaches. In Handbook of Beach and
941 Shoreface Morphodynamics; Short, A.D., Ed.; JohnWiley and Sons Ltd.: Chichester, UK, 1999;
942 pp. 230–250.

943 Soulsby, R. L., Hamm, L., Klopman, G., Myrhaug, D., Simons, R. R., & Thomas, G. P. (1993). Wave-
944 current interaction within and outside the bottom boundary layer. *Coastal Engineering*,
945 21(1-3), 41 – 69.
946 https://doi.org/10.1016/0378-3839(93)90045-a

947 Thom B. G., Eliot, I., Eliot, M., Harvey, N., Rissik, D., Sharples, C., Short, A. D. & Woodroffe, C. D.
948 (2018). National sediment compartment framework for Australian coastal management.
949 *Ocean and Coastal Management*, 154, 103 – 120.

950 Turner, J. F., Iliffe, J. C., Ziebart, M. K., Wilson, C., & Horsburgh, K. J. (2010). Interpolation of tidal
951 levels in the coastal zone for the creation of a hydrographic datum. *Journal of Atmospheric*
952 *and Ocean Technology*, 27(3), 605 – 613.
953 https://doi.org/10.1175/2009JTECHO645.1

954 Uncles, R. J. (2010). Physical properties and processes in the Bristol Channel and Severn Estuary.
955 *Marine Pollution Bulletin*, 61(1-3), 5– 20.
956 https://doi.org/10.1016/j.marpolbul.2009.12.010

957 Valiente, N. G., Masselink., G., Scott, T., Conley, D. C. & McCarroll, R. J. (2019a). Role of waves and
958 tides on depth of closure and potential for headland bypassing. *Marine Geology*, 407, 60 –
959 75.

960 Valiente, N. G., McCarroll, R. J., Masselink., G., Scott, T. & Wiggins, M. (2019b). Multi-annual
961 embayment sediment dynamics involving headland bypassing and sediment exchange across
962 the depth of closure. *Geomorphology*, 343, 48 – 64.
963 https://doi.org/10.1016/j.geomorph.2019.06.020

964 Valiente, N. G., Masselink., G., McCarroll, R. J., Scott, T., Conley, D. C. & King, E. V. (2020). Nearshore
965 sediment pathways and potential sediment budgets in embayed settings over a multi-annual
966 timescale. *Marine Geology*, 427, 106270.
967 https://doi.org/10.1016/j.margeo.2020.106270

968 van Rijn, L. C., Walstra, D. J. R. & van Ormondt, M. (2004). Description of TRANSPOR2004 and
969 implementation in Delft3D-ONLINE, Final Report. Report Z3748.10. Delft, The Netherlands:
970 WL Delft Hydraulics.

971 van Rijn, L. C. (2014). A simple general expression for longshore transport of sand, gravel and
972 shingle. *Coastal Engineering*, 90, 23 – 39.

973 van Rijn, L. C. (2007a). Unified view of sediment transport by currents and waves. I: Initiation of
974 motion, bed roughness, and bed-load transport. *Journal of Hydraulic Engineering*, 133(6),
975 649 – 667.
976 https://doi.org/10.1061/(ASCE)0733-9429(2007)133:6(649

977 van Rijn, L. C. (2007b). Unified view of sediment transport by currents and waves. II: Suspended
978 transport. *Journal of Hydraulic Engineering*, 133(6), 668 – 689.
979 https://doi.org/10.1061/(ASCE)0733-9429(2007)133:6(668

Vieira da Silva, G., Toldo, E. E., Klein, A. H. D. F., Short, A. D. & Woodroffe, C. D. (2016). Headland sand bypassing—Quantification of net sediment transport in embayed beaches, Santa Catarina Island North Shore, Southern Brazil. *Marine Geology*, 379, 13 – 27.

Vieira da Silva, G., Toldo, E. E., Klein, A. H. D. F. & Short, A. D. (2018). The influence of wave-, wind- and tide-forced currents on headland sand bypassing–Study case: Santa Catarina Island north shore, Brazil. *Geomorphology*, 312, 1 – 11.

Wiggins, M., Scott, T., Masselink, G., Russell, P. & McCarroll, R. J. (2019). Coastal embayment rotation: Response to extreme events and climate control, using full embayment surveys. *Geomorphology*, 327, 385 – 403. https://doi.org/10.1016/j.geomorph.2018.11.014

Willmott, C. J., Robeson, S. M., & Matsuura, K. (2012). A refined index of model performance. *International Journal of Climatology*, 32(13), 2088–2094. https://doi.org/10.1002/joc.2419

Young, I. R., Zieger, S., & Babanin, A. V. (2011). Global trends in wind speed and wave height. *Science*, 332(6028), 451 – 455. https://doi.org/10.1126/science.1197219

Appendices

Appendix A: Model parameters

Table A1: Hydrodynamic physical parameters.

Parameter	Value	Units
Horizontal eddy viscosity	1	$m^2 s^{-1}$
Horizontal eddy diffusivity	10	$m^2 s^{-1}$
Gravitational acceleration	9.81	$m s^{-2}$
Water density	1025	$kg m^{-3}$
Water temperature	15	°C
Salinity	35	PPT
Wave related bottom stress formulation	Fredsøe (1984)	-
Wind drag coefficients	$2e^{-3}$, 0, $7.23e^{-3}$, 100, $7.23e^{-3}$, 100	-,$m s^{-1}$
Air density	1	$kg m^{-3}$
Spiral motion	Included in 3D hydrodynamics	-
Bottom friction formulation	Manning	-
Bottom friction coefficient u, v	$2.75e^{-2}$, $2.75e^{-2}$	$s m^{-1/3}$
Drying/ flooding threshold depth	0.05	m

Table A2: Hydrodynamic numerical parameters.

Parameter	Value	Units
Computational time step	0.2	mins
Iterations in continuity equation	2	-
Number of sigma layers	10	-
Sigma layer thickness (surface – bed)	20,20,15,12,10,8,6,4,3,2	% depth
If depth < threshold, set whole cell to dry	YES	-
Depth determination at water level points when all vertices wet	MEAN	-
Depth determination at velocity points when all vertices wet	MEAN	-
Drying/ flooding threshold	0.05	m
Marginal depth in shallow areas	-999	m
Smoothing time at start of simulation	1440	mins
Numerical method for advective terms	Cyclic-method	-
Numerical method for momentum terms	Cyclic	-
Output storage time interval	60	mins
Communication time interval with WAVE	60	mins

1002

Table A3: Wave physical processes and parameters.

Process/ Parameter	Value	Units
Water level correction	0	m
Water levels	From FLOW	-
Currents	From FLOW	-
Gravitational acceleration	9.81	$m\ s^{-2}$
Water density	1025	$kg\ m^{-3}$
North direction	90°	Cartesian
Minimum depth	0.05	m
Physics	3rd Generation	-
Wave breaking	true	-
Alpha coefficient for wave breaking	1	-
Gamma coefficient for wave breaking	0.73	-
Non-linear triad interactions	true	-
Triad alpha proportionality coefficient	0.1	-
Triad beta max frequency ratio	2.2	-
Bed friction formulation	Madsen et al. (1988)	-
Bed friction coefficient	0.05	$m^2\ s^{-3}$
Diffraction	false	-
Wind growth	false	-
Whitecapping formulation	Komen (1984)	-

Quadruplets	false	-
Refraction	true	-
Frequency shifting	true	-
Method of wave force computation	dissipation 3d	-

Table A4: Numerical parameters in the CRM.

Process/ Parameter	Value	Units
Computational mode	Non-stationary	-
Computational time step	10	mins
Discretisation in directional space	0.5	-
Discretisation in frequency space	0.5	-
Relative change of wave height or mean wave period with respect to local value	0.05	-
Relative change of wave height with respect to model-wide average wave height	0.05	-
Relative change of mean wave period with respect to model-wide average mean wave period	0.05	-
Percentage of points for accuracy criteria satisfaction	98	%
maximum number of iterations	15	-
Directional resolution	10	°
Frequency min, max	0.05, 1	Hz
N frequency bins	24	-

Appendix B: Skill metrics

Skill was assessed using the following metrics: R^2, *BIAS*, mean absolute error *MAE*, Willmott Index of Agreement *WIA* and Brier Skill Score *BSS*. This appendix covers the calculation of the *BIAS*, *MAE*, *WIA*, and *BSS* metrics. *BIAS* was determined as:

$$BIAS = \frac{\sum_{i=1}^{n}(P_i - O_i)}{n}, \quad \text{(A1)}$$

Where P_i is the i^{th} model prediction and O_i is the i^{th} observed value, n is the total number of data points for comparison. *MAE* was determined as:

$$MAE = \frac{\sum_{i=1}^{n}(|P_i - O_i|)}{n}, \quad \text{(A2)}$$

WIA (Willmott et al., 2012) is given by:

$$d_r = \begin{cases} 1 - \dfrac{\sum_{i=1}^{n}|P_i - O_i|}{2\sum_{i=1}^{n}|O_i - \bar{O}|}, when \\ \sum_{i=1}^{n}|P_i - O_i| \le 2\sum_{i=1}^{n}|O_i - \bar{O}| \\ \dfrac{2\sum_{i=1}^{n}|O_i - \bar{O}|}{\sum_{i=1}^{n}|P_i - O_i|} - 1, when \\ \sum_{i=1}^{n}|P_i - O_i| > 2\sum_{i=1}^{n}|O_i - \bar{O}| \end{cases}, \quad \text{(A3)}$$

Where $\bar{P}$ and $\bar{O}$ are the mean prediction and observation, respectively. *WIA* varies from -1 to 1, indicating the magnitude of the summed predictive error relative to the summed observed deviations about the mean observation. A value >0 indicates the summed error magnitudes is less than the summed magnitude of the observed variation about the mean (by half for *WIA* = 0.5).

BSS is determined following Davidson et al., (2010) as:

$$BSS = 1 - \frac{\langle(|P_i - O_i| - \epsilon)^2\rangle}{\langle(|F_i - O_i|)^2\rangle} \quad \text{(A4)}$$

Where F_i represents the i^{th} value interpolated from a linear fit to the observation data and ϵ is the observation error. Observation errors used were 0.1 m for H_s, 1 s for T_p, 5° for direction and 0.02 ms^{-1} for currents, in accordance with McCarroll et al., (2018). Angle brackets represent the time mean.